Spring 5-16-2025

# TRANSITION METAL DISULPHIDE (Co, Ni, Fe) AS ELECTROCATALYST FOR OVERALL WATER SPLITTING

Urvashi Gondaliya
*Pittsburg State University*, urvashigondaliya209@gmail.com

TRANSITION METAL DISULPHIDE (Co, Ni, Fe) AS ELECTROCATALYST FOR
OVERALL WATER SPLITTING



Thesis Submitted to Graduate School
in Partial Fulfilment of the Requirements
for the Degree of
Master of Science



Urvashi Gondaliya



Pittsburg State University

Pittsburg, Kansas

May 2025

TRANSITION METAL DISULPHIDE (Co, Ni, Fe) AS ELECTROCATALYST FOR
OVERALL WATER SPLITTING


Urvashi Gondaliya


APPROVED:

Thesis Advisor     _____
                   Dr. Ram K. Gupta, Department of Chemistry


Committee Member   _____
                   Dr. Serif Uran, Department of Chemistry


Committee Member   _____
                   Dr. Timothy Dawsey, National Institute for Materials Advancement

# ACKNOWLEDGMENTS

Firstly, the foremost gratitude I would like to express to my research and program advisor Dr. Ram K. Gupta for his enormous support and guidance. His teaching methods led me to enrich my academic and research aptitude. His supervision and guidance led me to conduct my research productively and effortlessly. Moreover, Dr. Gupta supervised my direct training in various techniques and equipment in the laboratory, as well as generously offering his electrochemistry, battery, and polymer expertise. I would like to express many thanks for his mentorship and continuous encouragement to write and read about new scientific discoveries in the world outside my research scope. It updated my knowledge of the new scientific world and although it was challenging, the last two years of my Master program have been the most productive so far. Again, I would like to say thank you to him.

Secondly, I would also like to express my gratitude to my committee member, Dr. Serif Uran, for his guidance and recommendations, which significantly improved my thesis. I am thankful for the time he dedicated to supporting my academic work and for his invaluable insights.

Thirdly, I would also like to say thank you to Dr. Tim Dawsey who has been one of the pillars of the National Institute for Materials Advancement. He provided not only academic knowledge during research meetings but also guidance and support to succeed now and in my future academic endeavors.

Fourthly, I would like to thank Wang Lin for helping me during my thesis project. Also, Thank Felipe M. de Souza for the high-resolution SEM images of my materials.

# TRANSITION METAL DISULPHIDE (Co, Ni, Fe) AS ELECTROCATALYST FOR OVERALL WATER SPLITTING

An Abstract of the Thesis by
Urvashi Gondaliya

Increasing energy demands and environmental awareness have promoted extensive research on the development of alternative energy conversion and storage technologies that are both highly efficient and environmentally friendly. Among them, water splitting is very appealing, and it is considered as a good renewable and sustainable approach for the generation of green $H_2$ energy, however its implementation at industrial level is hindered due to the requirement of highly active and durable electrode material. Therefore, developing efficient electrocatalysts is of significant importance for high-performance water splitting. In the past few years, much effort has been devoted to the development of alternative electrocatalysts based on transition-metal elements that are low-cost, highly efficient, and have excellent stability. Herein, we developed Fe, Co, and Ni disulfides using microwave synthesis approach. The prepared materials were characterized by using analytical and spectroscopic techniques. Moreover, the prepared materials were evaluated for the electrochemical performance towards oxygen and hydrogen evolution reactions (OER and HER). Furthermore, catalytic activity for urea oxidation reaction (UOR) is also done for the rational treatment of urea. Among the synthesized catalysts, $NiS_2$ exhibited superior bifunctional activity with the lowest overpotentials for both OER (260 mV) and UOR (1.38 V), along with excellent stability and conductivity. $CoS_2$ demonstrated the best HER performance with an overpotential of 240 mV, while $FeS_2$ showed limited electrocatalytic activity due to its poor conductivity and low active site exposure. These

findings highlight the effectiveness of microwave-assisted synthesis for fabricating efficient and stable metal disulfide catalysts for water and urea electrolysis.

# TABLE OF CONTENTS

# LIST OF TABLES

# LIST OF FIGURES

# LIST OF ABBREVIATIONS

| | |
|---|---|
| FESEM | Field-emission scanning electron Microscopy |
| HER | Hydrogen evolution reaction |
| ESS | Energy storage system |
| LSV | Linear sweep voltammetry |
| PEM | Proton-exchange membrane water electrolysis |
| MW | Microwave |
| OP | Overpotential |
| UOR | Urea oxidation reaction |
| AEM | Anion-exchange membrane water electrolysis |
| XRD | X-ray diffraction |
| $C_{dl}$ | Electrochemical double-layer capacitance |
| ECSA | Electrochemical surface area |
| RF | Roughness factor |
| GSA | Geometrical surface area |

# CHAPTER I

# INTRODUCTION

One of the greatest demands in the world is the development of renewable and sustainable energy sources. Due to the fast growth in population over the last several years, there has been a significant increase in the amount of energy consumed, which has resulted in significant environmental issues [1,2]. The production of green oxygen ($O_2$) and hydrogen ($H_2$) using electrocatalytic water splitting is an exciting approach to meeting energy needs while also addressing environmental concerns. Hydroxides and sulfides of transition metals have recently been investigated as water splitting catalysts and as potential benchmark electrocatalysts for the oxygen evolution reaction (OER) and the hydrogen evolution reaction (HER), respectively [3-5]. The high price and limited availability on Earth limit their usefulness in many contexts. The slow kinetics in acidic and alkaline environments, together with the high voltage needed to drive the reaction process, especially for OER, restrict its broad range of applications. It follows that the likelihood of long-term, sustainable $H_2$ generation is highly dependent on OER kinetics, as this reaction typically follows a four-electron transfer route. Consequently, there has been a lot of focus on developing earth-abundant material catalysts that are highly active, inexpensive, and long-lasting for water splitting in general [6].

**1.1 Need for storage energy**
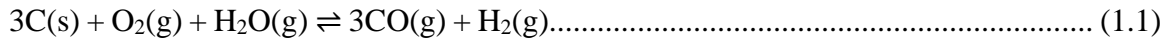
In order to maintain the equilibrium between energy production and energy consumption, an energy storage system (ESS) is used to store the energy that is generated and use it at a later time [7]. When it comes to meeting both the present and the future need for energy, the energy storage industry has been striving to create more ESSs. The demand for energy has grown as a result of the rapid advancements that have been made in the energy storage industry, as well as the huge growth in the general population throughout the world. In addition, it is essential to generate renewable energy sources in order to reduce the amount of carbon emissions that are generated by the combustion of fossil fuels, which is the major energy source that is currently being used in industry. There is a wide range of advantages that may be achieved by ESS [8]. In order to guarantee that customers will always have access to power, regardless of the applications for which it is used, ESS offers grid flexibility. The capacity to adapt to changing circumstances is essential for both dependability and resilience. It is becoming more important to have better resilience and dependability as the costs associated with outages continue to keep rising [9].

**1.2 Basics of overall water splitting**
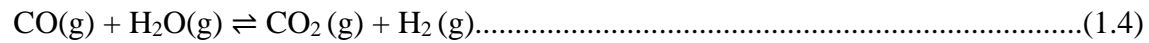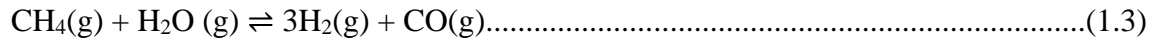
The term "water splitting" refers to the chemical process that occurs when water is divided into two gases: $H_2$ and $O_2$ [10]. The evolved $H_2$ may be used as fuel for fuel cells and vehicles, and it can also be compressed into a cryogenic liquid, which can then be transported and used in a variety of sectors. On the other hand, the $O_2$ that is created may either be discharged into the atmosphere or kept in liquid form for use in medical applications. There are three methods that have been used throughout history to split water

molecules: the gasification of coal, the steam methane reaction (SMR), and the electrolysis of water.
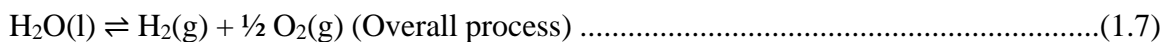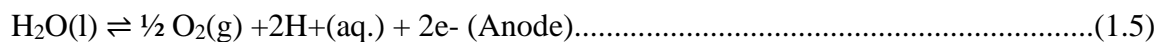
The process of thermochemically converting coal or biomass into carbon monoxide ($CO$) and $H_2$ gas, $CO$ and methane ($CH_4$) is known as coal gasification [12]. The gases that are produced by this process are collected on the surface. **Equation 1.1 & 1.2** shows the coal gasification process [13].

$$3C(s) + O_2(g) + H_2O(g) \rightleftharpoons 3CO(g) + H_2(g) \dotfill (1.1)$$

$$CO(g) + H_2O(g) \rightleftharpoons CO_2(g) + H_2(g) \dotfill (1.2)$$

When natural gas and water mix, the steam methane reaction takes place [14]. The initial products of this reaction are $Co$ and $H_2$ gas. Natural gas in this context refers to hydrocarbon $CH_4$. Following this stage, the process of reforming takes place, in which carbon monoxide is transformed into carbon dioxide and more $H_2$. **Equation 1.3 & 1.4** represents the SMR process.

$$CH_4(g) + H_2O\ (g) \rightleftharpoons 3H_2(g) + CO(g) \dotfill (1.3)$$

$$CO(g) + H_2O(g) \rightleftharpoons CO_2\ (g) + H_2\ (g) \dotfill (1.4)$$

In order for this reaction to take place, the temperature must be remarkably high (between 700 and 1000 $^0$ C) since it is an endothermic process that demands extra heat [15]. The process of electrolysis of water takes place when electricity is transferred through water, causing it to be broken down into $H_2$ and $O_2$ [16]. **Equation 1.5** depicts this reaction, which takes place at the anode and cathode of electrodes.

$$H_2O(l) \rightleftharpoons \tfrac{1}{2}\ O_2(g) + 2H^+(aq.) + 2e^-\ (\text{Anode}) \dotfill (1.5)$$

$$2H^+(aq.) + 2e^- \rightleftharpoons H_2(g)\ (\text{Cathode}) \dotfill (1.6)$$

$$H_2O(l) \rightleftharpoons H_2(g) + \tfrac{1}{2}\ O_2(g)\ (\text{Overall process}) \dotfill (1.7)$$

Different techniques may be used to electrolysis of water, including proton-exchange membrane water electrolysis (PEM), anion-exchange membrane water electrolysis (AEM) and traditional water electrolysis in aqueous solution [17].

Anion-exchange membrane water electrolysis is one low-cost electrolysis method, and it is still in the process of development. It is necessary to have an exchange membrane that allows the movement of anions via its surface in order to conduct this process. During this process, water breaks down into hydrogen ions ($H^+$) and hydroxyl ($OH^-$) ions at the cathode. These $OH^-$ ions then go towards the anode, where they form $O_2$ gas [18]. At the industrial level, AEM continues to struggle with a few barriers, the most significant of which is having membrane durability at a low current density.

The electrolysis of water using a proton exchange membrane produces the cleanest form of $H_2$ gas, in addition to ensuring that the environment is clean and provides improved safety. The membranes that are used in this process are solid electrolytes. These membranes are often composed of polymers that are placed between layers of catalysts. This allows $H^+$ ions to go across the membrane, which results in the production of $H_2$ gas at the cathode. The fluctuations in temperature that occur during PEM have an effect on all of the parameters of water electrolysis. This, in turn, necessitates the implementation of a water management system, which leads to an increase in the application cost [19].

In conventional water electrolysis, which takes place in an electrolyte solution $H_2$ evolved at the cathode. This process is known as HER and it is used to describe the development of $H_2$. At the same time, the anode is responsible for the production of $O_2$ gas, which is referred to as the OER [20].

**1.3 Hydrogen energy**

Green $H_2$ energy is a perfect energy option to replace fossil fuels and address the present energy crisis we are facing [21]. Compared to contemporary electric automobiles, $H_2$ fuel cell-powered vehicles offer many benefits. $H_2$ fuel cell cars have exceptional endurance and can replace $H_2$ quickly. The primary impediment to the advancement of $H_2$ energy cars is the exorbitant expense associated with producing green $H_2$ energy. There are a few ways to produce it, but the most effective one is water electrolysis, which calls for environmentally friendly electricity produced by solar or wind power [22-24]. Given the circumstances, this technique may be less harmful and carbon-free. The primary causes of green $H_2$ energy's high cost are water electrolysis catalysts and electricity. The capacity of catalysts to lower the energy required for reactions makes them essential for electrochemistry. Therefore, the main focus of research in this field is on developing affordable and effective electrocatalysts in order to achieve widespread generation of green $H_2$ energy. The overall reaction of water electrolysis can be divided into two half-cell reactions: HER and OER [25,26].

**1.3.1 Hydrogen evolution reaction**

The process by which water is reduced at the cathode to produce $H_2$ is known as the HER. The only difference between the HER process in acidic and alkaline environments is the supply of protons. Regarding the proton source, in an acidic environment, the three primary types of reaction mechanisms for the HER are the Heyrovsky reaction, the Tafel reaction, and the Volmer reaction [27]. The electrochemical desorption phase and the electrochemical adsorption phase are represented by the Heyrovsky and Volmer reactions, respectively. An adsorbed hydrogen atom is formed

when a proton gains electrons via electron transfer, and it then combines with protons in the electrolyte. The catalyst-adsorbed hydrogen atoms combine to form $H_2$ gas in the third Tafel reaction, which is a phase in the composite desorption process. Electron transfer and desorption are the two phases that make up the complete HER as seen through the lens of the HER reaction mechanism. The Tafel slope's magnitude provides information about electrochemical reaction kinetics. The adsorption and desorption of hydrogen atoms on the catalyst surface are two competing processes that take place during the HER. $H_2$ may develop quickly but is not discharged well if the adsorption is strong. $H_2$ production is challenging but easy to discharge if the adsorption is too weak. The catalytic activity toward the hydrogen evolution reaction (HER) is often evaluated using the Gibbs free energy of hydrogen adsorption ($\Delta G\_H$), which serves as a key thermodynamic descriptor. An optimal HER catalyst exhibits a $\Delta G\_H$ value close to zero, indicating a favorable balance between hydrogen adsorption and desorption on the catalyst surface. This principle is commonly illustrated through a 'volcano plot', where materials with $\Delta G\_H$ values approaching zero typically reside at the peak, reflecting their superior catalytic performance. Deviations from this equilibrium, either through overly strong or weak hydrogen binding, can significantly hinder HER kinetics. [28,29]. There are two primary categories of HER electrocatalysts, which are known as noble-metal-based electrocatalysts and non-noble metal-based electrocatalysts. A comparison is made between these catalysts with regard to the electrocatalytic performance and the kinetic parameters under a variety of different environmental conditions. In the case of electrocatalysts based on noble metals, particularly those based on platinum, a number of different techniques are now being explored in order to improve the performance of HER and reduce the cost of

electrocatalysts [30]. One example is that the use of platinum might be improved by alloying it with other low-cost transition metals. Additionally, the synergistic impact of alloy could affect the electrical surroundings, which would result in an improvement in activity. Additionally, combining platinum with other water dissociation promoters is a significant technique for improving HER alkaline activities, which is particularly relevant for the practical application of the industry. Because of the cheap cost and earth-abundant properties of non-noble metal-based HER electrocatalysts, a significant amount of attention has been directed to their development. This is mostly due to the fact that these traits are considered to be advantageous. Several kinds of non-noble metal-based electrocatalysts, including transition metal carbides, transition metal phosphides, and transition metal chalcogenides, have seen significant progress in the area of electrocatalytic HER [31-33]. Among them, Pt-based precious metals have moderate $H_2$ adsorption free energy, and experiments have also proved that they have high HER rate and catalytic activity. However, Pt-based materials are not practical for large commercial use due to their rare and expensive nature. Therefore, it is important to explore catalysts with moderate $H_2$ adsorption free energy or optimize existing materials for this purpose.

**1.3.2 Oxygen evolution reaction**

The anode of electrolyzed water is where the OER takes place. The multi-electron transfer method used in the OER process has a sluggish reaction rate and a high overpotential, which results in the high energy consumption of electrolyzed water and limits its commercial growth [34]. Noble-metal-based and non-noble metal-based OER electrocatalysts are the two primary categories of these catalysts. Ru and Ir-based catalysts are thought to be the most advanced noble metal based OER catalysts, particularly in the

acidic electrolyte, where they have a higher dissolution resistance than other metals. Numerous methods exist for engineering and optimizing the catalyst composition, structure, and morphology in order to lower the high cost, enhance electrocatalyst activity and stability, and even enforce the dissolving resistance in acidic medium [35-37]. Apart from Ir and Ru, bi or tri-functional electrocatalysts based on noble metals, such Rh, Au, Pt, and Pd, have also been produced. The earth-abundant oxide, sulfides, and hydroxide electrocatalysts, which are based on non-noble metals, have gathered significant attention for their OER properties. Of these, Ni–Fe-Co based oxide and hydroxide are among the most frequently used OER catalysts in industrial-scale. OER is the second important half-reaction in the water-splitting process, as was previously mentioned. In contrast to HER, this reaction takes place at the anode and needs a surprisingly high overpotential due to its four-electron transfer method. The main obstacle to raising electrochemical water splitting's overall efficiency is recognized to be OER [38]. Consequently, it is critical to look for OER catalysts with high efficiency that may successfully lower the kinetic limit. The knowledge of the OER mechanism has recently advanced significantly, allowing for the logical design of OER electrocatalysts. [39,40].

### 1.3.3 Urea oxidation reactions

In the field of $H_2$ production, water splitting is often regarded as the most effective method. The sustainable cycle may be achieved by combining water splitting with the methods of $H_2$-$O_2$ fuel cells [41]. When it comes to the alternative processes, it has been shown that the oxidation of ammonia, alcohol, glucose, and urea are all useful in helping water splitting with low overpotential and energy input [42]. In particular, it has been observed that urea is an excellent hydrogen transporter, as it contains a significant amount

of hydrogen at 6.67% by mass [43]. Furthermore, the non-toxic products of $N_2$ and $CO_2$ that are produced by the urea oxidation reaction (UOR) are able to prevent the simultaneous mixing of $H_2$ and $O_2$. Particularly noteworthy is the fact that the theoretical voltage of urea electrolysis is just 0.37 V vs. RHE, which is far lower than the 1.23 V that is required for water splitting [44]. Additionally, urea is a frequent environmental pollutant that is emitted from agricultural fertilizer, industrial production, and residential excretion. As a result, urea-assisted water splitting not only provides clean hydrogen energy but also reduces the amount of pollution that is released into the environment. Wastewater containing organic urea is dumped straight into the environment without being treated, which results in significant contamination of the ecosystem. In addition, urea has the ability to spontaneously degrade into ammonia, which is a gas that is toxic. Human health will be harmed by gas, regardless of whether it is regulated or cleaned. In addition to being an efficient technique for the rational treatment of urea, UOR is also a technology that is capable of producing $H_2$ via electrolysis.

$$CO(NH_2)_2 + H_2O = N_2 + 3H_2 + CO_2 \dots\dots\dots\dots\dots\dots\dots\dots\dots\dots\dots\dots\dots\dots..\dots(1.8)$$

Therefore, it is essential to take a reasonable approach to the development of a catalyst that can catalyze the UOR [45].

Both the anode oxidation of the urea molecule and the cathode HER are considered to be components of the urea-assisted water splitting process, as was previously described. In contrast to the HER, the UOR also encounters the challenge of sluggish reaction kinetics due to the 6 e− transfer process. As a result, extremely effective catalysts are required to significantly increase catalytic kinetics. Catalysts based on noble metals, such as platinum and ruthenium, display a significant amount of catalytic activity; nevertheless, their

availability and cost are restricting their use. To our good fortune, the electrocatalysts based on transition metals exhibit a moderate level of activity for UOR. When compared to other transition metals (such as cobalt, iron, manganese, and so on), catalysts based on nickel have been shown to be very promising and robust for the oxidation of urea [46].As a result of its earth abundance, high stability in strong alkaline media, and the ease with which active phase production may occur as a consequence of multivalent oxidation states, Ni-based UOR electrocatalysts have garnered an increasing amount of interest.

## 1.4 Object of thesis

Composites based on transition metal sulfides have attracted a lot of attention due to the fact that they have the potential to be used as electrode materials in energy conversion and storage applications. This is because of their extraordinary qualities, which include a large number of active sites and properties that can be adjusted. On the other hand, these materials also provide a number of problems, such as delayed charge carrier transport kinetics, restricted electrochemical surface area, and inferior performance in electrochemical processes. As a result, microwave synthesis has been used in order to overcome these limits. These techniques have been implemented with the intention of addressing concerns such as material shrinkage, inadequate substrate contact, low-rate capability, and insufficient energy density. Within the scope of this investigation, the primary objective was to improve the efficiency and stability of sulfides-based transition metal for the purpose of energy conversion.

To begin with, an efficient synthesis technique was used in order to manufacture nanostructured materials that had well defined morphologies. This resulted in an increase in both the surface area and the porosity of the materials. Subsequently, efforts were

concentrated towards overcoming remaining constraints and increasing characteristics, with the goal of use in a new era in the field of sulfide-based material research. Several structural and electrochemical characterizations were conducted on the transition of metal sulfide materials in order to conduct analysis of these materials. Insights into the material's composition, crystalline structure, surface morphology, and electrochemical behavior were supplied by these investigations.

This allowed for a more in-depth comprehension of the material's performance as well as its potential for use in energy conversion and storage devices. In addition, efforts were made to investigate innovative methodologies and techniques for further strengthening the characteristics and usefulness of metal oxide composites. The goal was to solve the issues that are currently being faced and to open up new potential for the application of these materials in advanced energy technology.

# CHAPTER II

## EXPERIMENTAL DETAILS

### 2.1. Materials

Iron (lll) nitrate nonahydrate from high purity grade was purchased from ACROS Organic (New Jersey, USA). Cobalt (ll) nitrate hexahydrate and nickel (ll) nitrate hexahydrate were purchased from Strem Chemicals (New Buryport, USA). Urea (99.9%) and sulfur were purchased from Acros Organics (New Jersey, USA). Distilled water was purchased from the local Walmart (Pittsburg, KS). Nickel foams were obtained from MTI-KJ Group (Richmond, CA). 1-methyl-2-pyrrolidone was purchased from Fisher (New Jersey, NJ), and polyvinylidene fluoride (PVDF) was purchased from Sigma-Aldrich (St. Louis, MO) which were used to make the electrodes.

### 2.2. Synthesis of $CoS_2$, $NiS_2$ and $FeS_2$

For the synthesis of metal sulfides ($CoS_2$, $NiS_2$ and $FeS_2$) through microwave method, 1 mM cobalt (II) nitrate hexahydrate ($Co (NO_3)_2.6H_2O$) and 4 mM Urea dissolved in 20 ml of deionized water. Subsequently, the solution underwent sonication using a sonic machine for 5 min. The solution was then transferred to a 35ml Pyrex microwave vial and subjected into microwave reactor at 160°C for 10 minutes. The compound formed was separated through centrifugation. Following the reaction, the synthesized material was rinsed with deionized water and dried in an oven at 60°C for 24 hours. The dried product

along with sulfur was placed in tube furnace at 450°C for 1 h under Ar atmosphere to obtain $CoS_2$. The same procedure was applied for nickel (II) nitrate hexahydrate (Ni $(NO_3)_2.6H_2O$) and iron (III) nitrate nonahydrate (Fe $(NO_3)_3.9H_2O$).
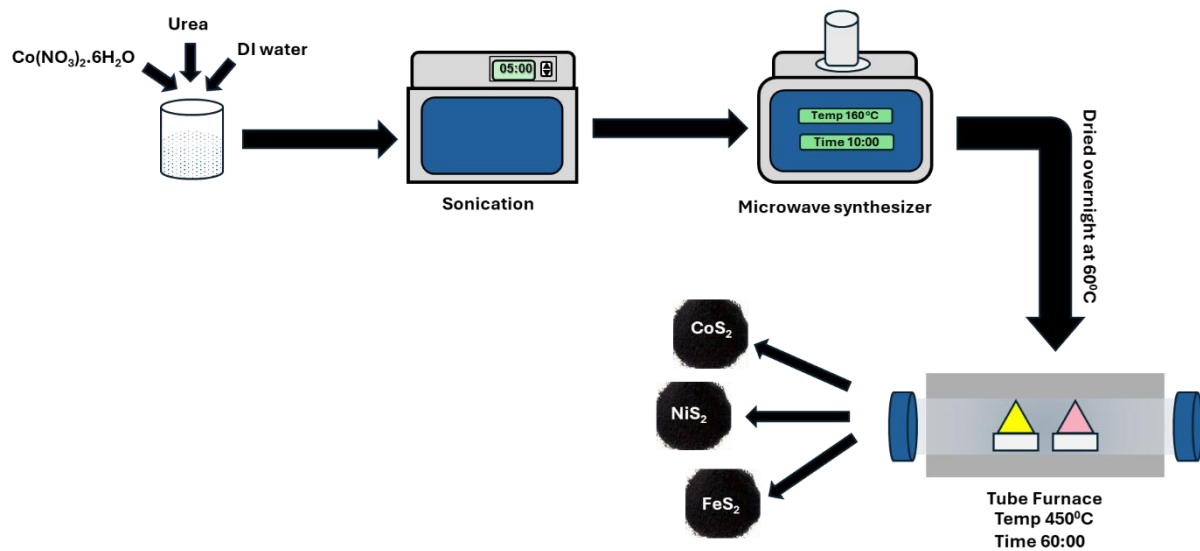


**Figure 1:** A schematic representation of a preparation of $CoS_2$, $NiS_2$ and $FeS_2$ by microwave approach

## 2.3. Preparation of electrodes

To make the working electrodes for the $CoS_2$ sample. First, Ni foam was washed and then sonicated in water for 10 min, and finally in acetone for 10 min before drying in an oven for 1 h at 70 °C. In the meantime, 2 mg of PVDF was weighed followed by the addition of 10 to 15 drops of 1-methyl-2-pyrrolidone, an organic binder which was placed in the oven to dissolve the PVDF. After that, 2 mg of acetylene black, followed by 16 mg of sample, were added to the mixture. The components were grinded until they became a fine and homogeneous paste that was used to coat the surface of the Nickel foam. The coated Nickel foams were dried in vacuum oven at 70°C for 48 hours. Also to make electrodes for $NiS_2$ and $FeS_2$ the same procedure was followed.

## 2.4. Physical characterization

The crystalline phase of the $CoS_2$, $NiS_2$ and $FeS_2$ was identified by X-ray diffractometer (XRD) XRD-6000 equipped with a Cu-Kα as a source, wavelength of 1.54 Å, and 2θ degree from 10 to 80. The morphology and structure of synthesized metal-based sulfides material were investigated by using a field emission scanning electron microscope (FESEM) Hitachi SU 5000 coupled with an energy dispersive X-ray (EDX) from Oxford Instruments.

## 2.4.1. Scanning electron microscopy

In order to examine the shape of the produced materials, field-emission scanning microscopy (FE-SEM) was used. The electron beams that bombarded the sample interacted with the electrons released by the sample, allowing us to detect its surface details. The X-rays, Auger electrons, backscattered electrons, and secondary electrons are only a few of the signals that come from this interaction.

Specifically, all imaging was performed at 10 keV and the morphology and topography were evaluated by detecting secondary electrons. The analysis of backscattered electrons, meanwhile, revealed the samples' elemental mapping. A field emission cathode or tungsten filament is the typical electron source used in scanning electron microscopes to produce an electron beam. The sample under investigation is accelerated to receive these electrons. A network of electromagnetic lenses controls and concentrates the electron beam as it travels through the system. An electron beam is focused on a small, concentrated point by controlling its size and shape via an aperture. To prevent electrons from being scattered and molecules of air from being absorbed, the substance to be investigated is placed in a vacuum chamber. Installing detectors in the chamber allows for the collection of various signals emitted or scattered by the sample.

An electron beam is over the surface of the sample using electromagnetic scanning coils. The whole surface of the sample may be scanted in a systematic way thanks to these coils, which move the beam both horizontally and vertically. Photons, which are another byproduct of electron interaction with the sample, may provide further insight into the material's properties. After the electron beam interacts with the substance, a number of detectors capture the resulting signals. After processing the data from the detectors, images displaying the surface shape and chemical composition of the sample are generated. You may see these pictures on a screen [47,48].
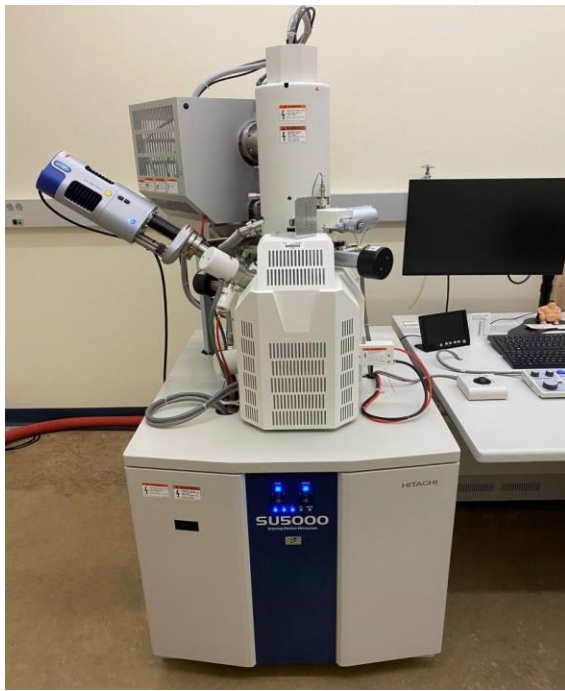
**Figure 2:** Schematic of SEM and the digital image of FESEM (SU 5000 - Hitachi) used in this research.

### 2.4.2. X-ray diffraction

X-ray diffraction (XRD) is an effective tool for studying materials down to the molecular level. Both crystalline and amorphous samples interact with X-rays during XRD, which cause X-ray scattering in different directions according to the sample's atomic or molecular organization. An X-ray tube often has a filament that releases electrons that are driven at high voltage toward a metal target, such copper or cobalt, in order to create these X-rays. Electrons use a mechanism called Bremsstrahlung radiation to generate X-rays when they hit a target. Typically, the sample crystalline powder or a hybrid of amorphous and single-crystal powder is illuminated by the concentrated monochromatic X-ray beam. Electron clouds around atomic nuclei interact with incoming X-rays, causing them to scatter when they meet with atoms or molecules in the sample. Different types of

16

constructive and destructive interference between scattered X-rays may be seen, depending on the incoming X-rays' wavelength and the angle of dispersion. An analysis of the structure and phase of crystalline or amorphous materials was conducted using Bragg's rule ($2d \sin\theta = n\lambda$), where n is the order of reflection, $\lambda$ is the wavelength of X-rays, d is the inter-planner spacing, and T is the diffracted angle. On the other side of the sample is a detector that gathers the diffracted X-rays. Rotating the sample and adjusting the angle of incidence ($\theta$) may produce diffraction patterns that include various scattering angles. If you want to know how the atoms are arranged, the crystallographic orientation, and the structural properties of a substance are, then X-ray diffraction is the way to go [49].



**Figure 3:** Digital images of Shimadzu X-ray diffractometer used in this research.

**2.5. Electrochemical measurement**

All electrochemical tests were conducted at ambient room temperature using a PARSTAT MC electrochemical workstation from Princeton Applied Research, USA. The experiments were conducted in conventional three-electrode systems, with 1M KOH serving as the electrolyte solution. In these setups, the working electrode consisted of Ni-foam coated with the synthesized transition-based metal sulfides. Platinum wire served as the counter electrode, while a saturated calomel electrode (SCE) or Hg/HgO electrode was utilized as the reference electrode in the investigation of its performance in water splitting, and urea oxidation, as well as in assessing its characteristics. The study assessed electrocatalytic activity based on surface area and active sites, without considering the mass loading of the material directly applied to Ni-foam, which was not the study's main objective. Recognizing the relevance of this parameter in electrochemical studies [50], we then assessed the material's mass loading on the Ni-foam.

In the investigation of its electrocatalytic properties, a comprehensive potentiodynamic study was conducted using linear sweep voltammetry (LSV). These experiments were conducted in a 1 M KOH electrolyte solution. Notably, all measured potentials were adjusted to the reversible hydrogen electrode (RHE) to ensure consistency and comparability across measurements. Specifically, in the case of LSV, a crucial step involved iR compensation to correct for any potential drop caused by the electrolyte resistance. Following this compensation, the LSV measurements were processed using the formula: $E_{RHE} = E_{Hg/HgCl2} + 0.059 * pH - iR$. This adjustment ensured accurate determination of the electrode potential relative to the RHE reference.

**Figure 4:** Images of (a) three electrode configurations, (b) the digital image of PARSTAT MC electrochemical workstation used in this research.

# CHAPTER III

## RESULT AND DISCUSSION

### 3.1. Structure and characterization

### 3.1.1. X-ray diffraction

The structural composition, crystallinity, and phase purity of the synthesized cobalt disulfide ($CoS_2$), iron disulfide ($FeS_2$), and nickel disulfide ($NiS_2$) were thoroughly examined using powder X-ray diffraction, and the resulting patterns are presented in **Figure 5.** The XRD results confirm the formation of crystalline, single-phase cubic pyrite structures for all three materials. The measured diffraction peaks match closely with the standard reference patterns of JCPDS card numbers #96-154-4895 for $CoS_2$ , #96-901-5843 for $FeS_2$, and #96-901-2539 for $NiS_2$. The absence of secondary peaks across all patterns validates the phase-pure synthesis.

For $CoS_2$, distinct and sharp peaks were observed at $2\theta = 27.9°$, $32.3°$, $36.3°$, $39.7°$, $46.3°$, $54.8°$, $56.3°$, $61.5°$, $63.6°$, $68.2°$, $72.2°$, $75.3°$, $77.7°$, and $79.6°$, which correspond to the (111), (200), (210), (211), (220), (300), (311), (222), (320), (321), (400), (411), (332), and (420) planes, respectively. These peaks reflect the typical face-centered cubic pyrite structure of $CoS_2$ with high crystallinity. The prominent intensity of the (220) and (311) reflections suggest preferred orientation and excellent long-range ordering [50].

The XRD pattern of $FeS_2$ confirms the formation of a pure cubic pyrite structure, consistent with JCPDS card no. 96-901-5843. The diffraction peaks appear at $2\theta = 28.1°$, $32.9°$, $37.1°$, $40.7°$, $47.3°$, $54.9°$, $56.2°$, $61.8°$, $63.9°$, $68.5°$, $72.6°$, $75.6°$, $78.1°$, and $79.8°$, corresponding to the (110), (200), (210), (211), (220), (300), (311), (222), (320), (321), (400), (411), (332), and (420) planes, respectively. The presence of higher-index reflections, particularly above 70°, along with the absence of impurity peaks, indicates a high degree of crystalline and phase purity [51].

In the case of $NiS_2$, the XRD pattern shows distinct reflections at $2\theta = 27.9°$, $32.3°$, $36.4°$, $40.0°$, $46.4°$, $54.8°$, $56.5°$, $61.6°$, $63.7°$, $68.2°$, $72.2°$, $75.3°$, $77.6°$, and $79.3°$, which are assigned to the (111), (200), (210), (211), (220), (300), (311), (222), (320), (321), (400), (411), (332), and (323) planes. The pattern corresponds well with JCPDS card no. 96-901-2539, confirming the formation of a phase-pure cubic pyrite $NiS_2$. The strong intensities of the (two hundred), (220), and (311) peaks further indicate the high crystalline and uniform atomic arrangement of the synthesized material [52].

Taken together, the XRD data presented in **Figure 5.** confirm that the synthesized $CoS_2$, $FeS_2$, and $NiS_2$ materials possess highly crystalline, phase-pure cubic pyrite structures with no observable impurities. The close match with standard JCPDS files and agreement with multiple literature sources strongly support the structural identity of the materials, laying a solid foundation for their subsequent evaluation in electrocatalytic systems.
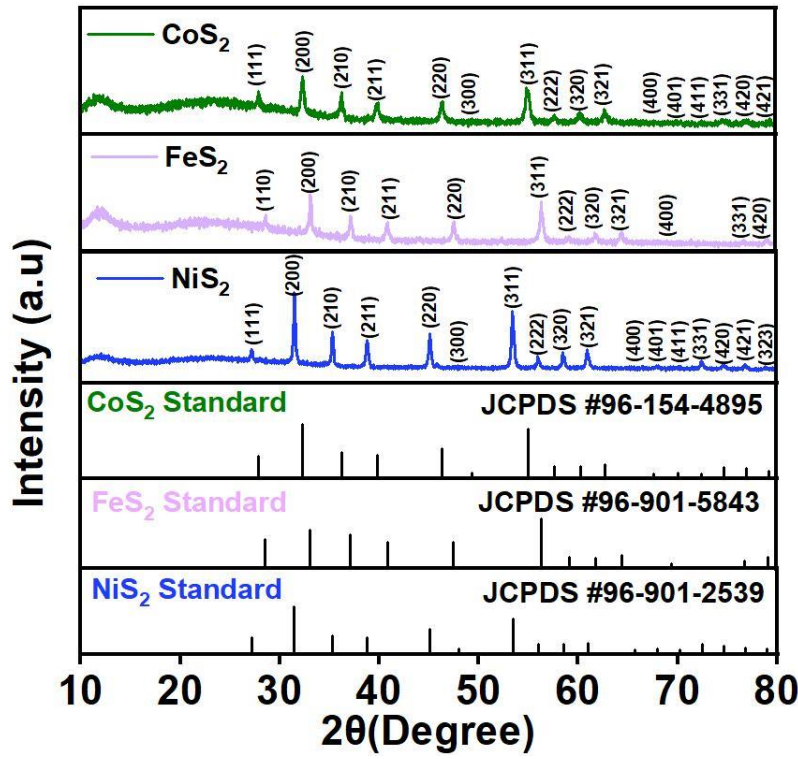
**Figure 5:** XRD patterns of $CoS_2$, $NiS_2$ and $FeS_2$

### 3.1.2. Scanning electron microscopy

The surface morphology and microstructure of the synthesized $CoS_2$, $NiS_2$, and $FeS_2$ were examined using field emission scanning electron microscopy, as shown in **Figures 6 to 8**. $CoS_2$ microstructures **(Figures6a-c)** reveal agglomerate spherical particles with a rough surface texture, forming dense clusters across the substrate. At higher magnification **(Figure 6b)**, the particles exhibit hierarchical morphology, suggesting a flower-like or cauliflower-like architecture, which enhances surface area and could improve catalytic activity due to increased active sites [53-55]. Elemental mapping **(Figure 6c)** confirms a uniform distribution of Co and S elements, indicating homogeneity and successful sulfidation. Such micro spherical morphologies have been associated with superior electrocatalytic performance in HER applications [54].

22
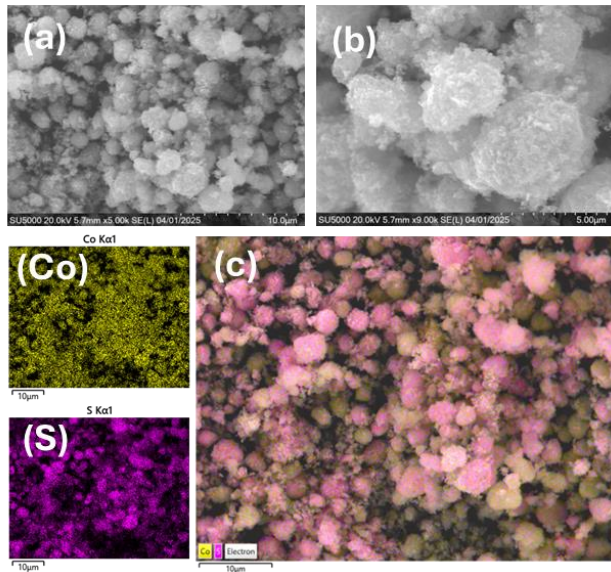
**Figure 6:** Morphological analysis of $CoS_2$ through SEM at different magnifications along with elemental mapping.

NiS$_2$ structures **(Figures 7 a–c)** exhibit a densely packed nanosphere morphology, with well-defined granular features across the surface. The particles are smaller and more uniformly distributed than those in $CoS_2$, as seen in both 10 µm and 5 µm scale images **(Figures 7a and 7b)**. This nanoscale arrangement is beneficial for fast charge transfer during electrochemical reactions. The EDX mapping **(Figure 7c)** reveals strong co-localization of Ni and S, suggesting the successful formation of stoichiometric $NiS_2$. Previous reports have linked this type of nano-granular surface morphology to enhanced conductivity and long-term stability in electrocatalytic processes [56-58].
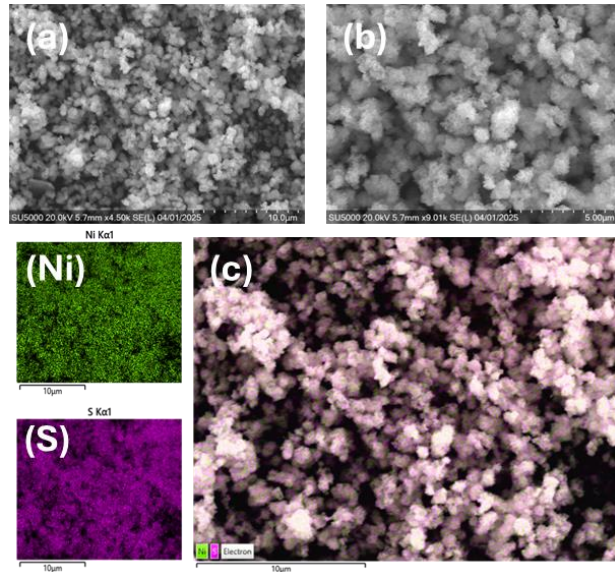
**Figure 7:** Morphological analysis of NiS$_2$ through SEM at different magnifications along with elemental mapping.

In the case of FeS$_2$ **(Figures 8a-c)**, morphology displays a mix of irregular flake-like and block-shaped particles. The lower magnification SEM **(Figure 8a)** shows larger micro flakes dispersed among finer particulates, while high magnification **(Figure 8b)** reveals the flat, plate-like nature of these flakes [59] . Elemental mapping **(Figure 8c)** clearly confirms the uniform presence of Fe and S across the sample, validating successful synthesis. Literature suggests that these heterogeneous morphologies are advantageous for multi-step redox reactions due to varied active site environments [60].
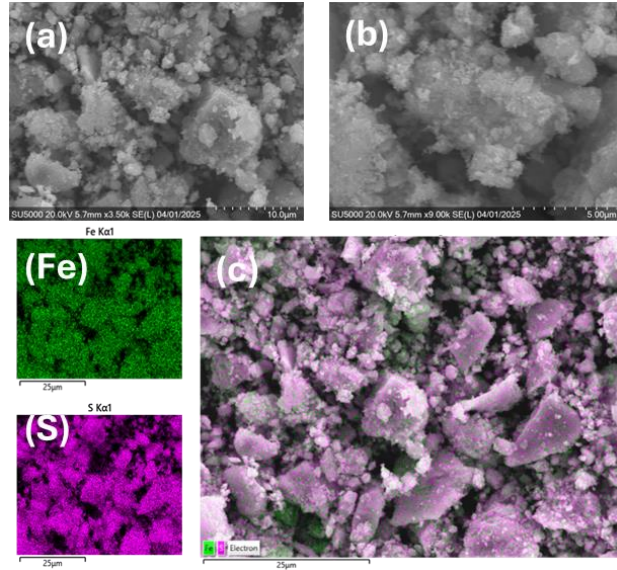
**Figure 8:** Morphological analysis of FeS$_2$ through SEM at different magnifications along with elemental mapping.

## 3.2. Electrocatalytic performances

### 3.2.1. Oxygen evolution reaction

The synthesized transition metal disulfides CoS$_2$, NiS$_2$, and FeS$_2$ were electrochemically evaluated for their oxygen evolution reaction activity in 1.0 M KOH solution using linear sweep voltammetry. As displayed in **Figure 9(a)**, the polarization curves show that the overpotentials required to achieve a current density of 10 mA·cm$^{-2}$ were 260 mV for NiS$_2$, 270 mV for CoS$_2$, and 300 mV for FeS$_2$. These results clearly highlight that NiS$_2$ exhibits the highest OER activity, followed by CoS$_2$, while FeS$_2$ shows lower performance. The improved electrocatalytic performance of NiS$_2$ can be attributed to its nanostructured, highly dispersed surface morphology, as revealed by SEM images **(Figures 7a-c)**. The nanoscale particle size and uniform distribution creates a larger electrochemically active surface area, enabling more reaction sites to participate in the oxygen evolution reaction [61,62]. Additionally, such morphology enhances interaction with the electrolyte, shortens ion diffusion pathways, and allows rapid oxygen bubble

25

detachment, thereby minimizing electrode passivation during the reaction [63]. $NiS_2$ has also been previously reported to exhibit good structural stability and conductivity in alkaline media, making it an ideal non-noble electrocatalyst for OER [64]. $CoS_2$, while requiring a slightly higher overpotential (270 mV), still demonstrates competitive OER activity. The SEM images **(Figures 6a–c)** reveal agglomerated micro-spherical clusters, which, although larger in size, offer a hierarchical roughness that facilitates electrolyte contact and provides multiple active sites. However, excessive clustering can hinder the accessibility of inner sites, thus slightly reducing the utilization efficiency compared to $NiS_2$. Despite this, $CoS_2$ remains a strong OER candidate due to its robust phase stability and metallic nature, which contributes to efficient charge transfer during the catalytic process [65]. In contrast, $FeS_2$ exhibited the highest overpotential (300 mV), indicating lower OER performance under the same testing conditions. SEM images **(Figures 8a-c)** show block-like and flake-shaped particles with larger sizes and irregular morphology, resulting in fewer exposed active sites. The bulky structure restricts electrolyte penetration and may increase resistance to charge transport [66]. Furthermore, $FeS_2$ has lower inherent conductivity compared to $NiS_2$ and $CoS_2$, which can lead to reduced electron mobility and sluggish OER kinetics [67]. Despite this, Fe-based sulfides remain attractive due to their abundance, environmental friendliness, and low cost, and their performance can be significantly improved through doping or nano structuring strategies [68].

The Tafel slopes related to the OER performance of the disulfides electrocatalysts were obtained as shown in **Figure 9(b)** The Tafel slope can be calculated based on **Equation 3.1** and plotting the steady state of the polarization curves on the linear region.

$$\eta = a + \left(\frac{2.303RT}{\alpha nF}\right) \times \log j \,\ldots\ldots\ldots\ldots\ldots\ldots\ldots\ldots\ldots\ldots\ldots\ldots\ldots\ldots\ldots\ldots\ldots\ldots\ldots\ldots\ldots\ldots(3.1)$$
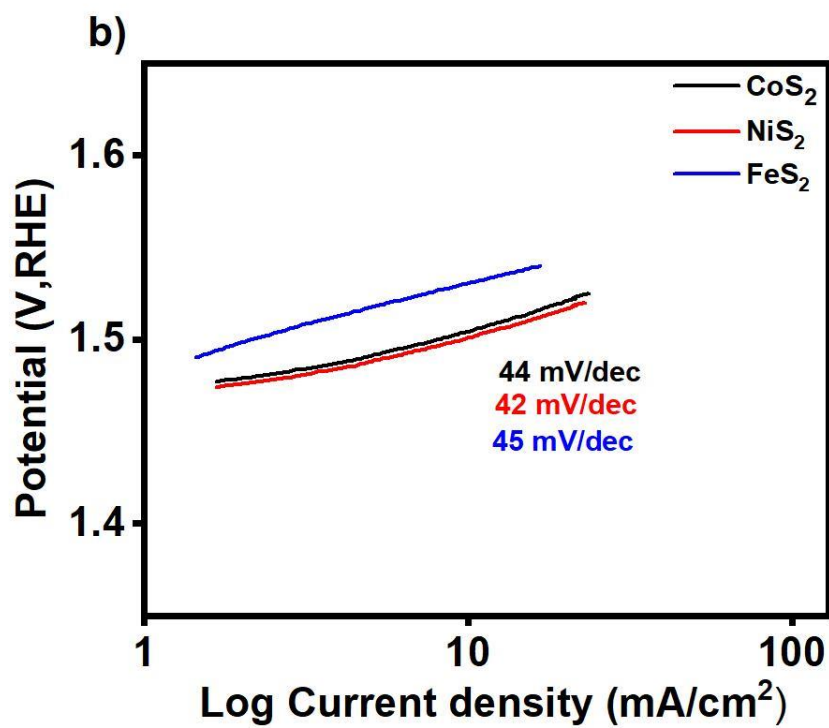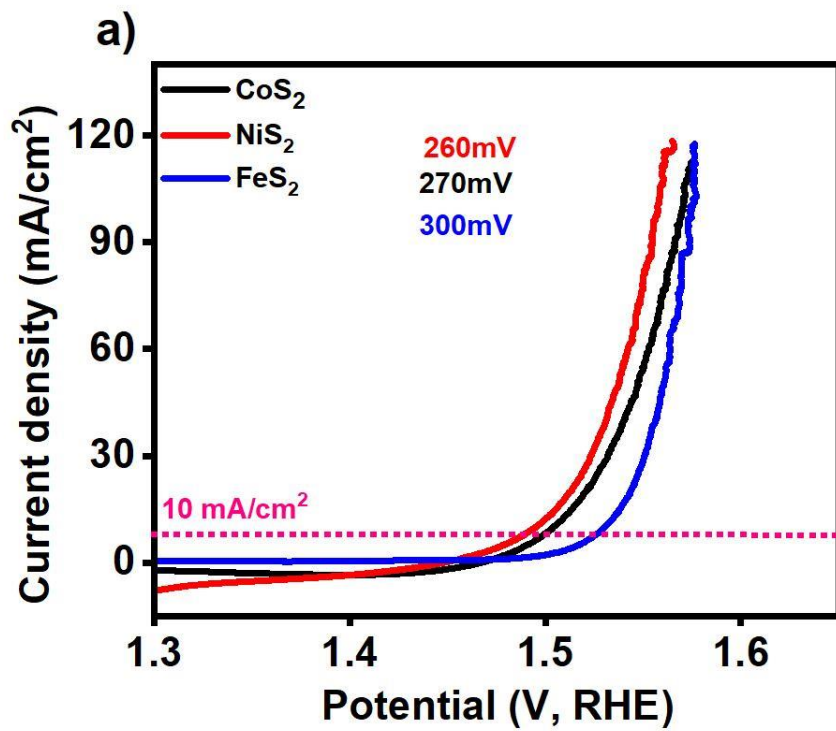
Where $\eta$ is the overpotential, n is the number of e$^-$ in the reaction, which is four for OER, $\alpha$ is the charge transfer coefficient, j is current density, and F is the Faraday constant. The Tafel slope can be given by $\left(\frac{2.303RT}{\alpha nF}\right)$. The calculated Tafel slopes were 42 mV/dec for $NiS_2$, 44 mV/dec for $CoS_2$, and 45 mV/dec for $FeS_2$, respectively. A smaller Tafel slope indicates faster reaction kinetics, meaning that a slight increase in overpotential results in a larger increase in current density. Among the three, $NiS_2$ exhibits the lowest Tafel slope, demonstrating that it possesses the most favorable OER kinetics.

This result directly correlates with the overpotential trend discussed in **Figure 7(a)**, where $NiS_2$ also showed the lowest overpotential (260 mV) at 10 mA/cm². The improved kinetic behavior of $NiS_2$ can be attributed to its nanoscale, well-dispersed morphology, as observed in SEM images, which enhances ion accessibility and accelerates charge transfer at the electrode–electrolyte interface [62]. Furthermore, the interconnected nanostructure minimizes internal resistance and enables more efficient electron transport, contributing to both lower overpotential and a more favorable Tafel slope [69].

$CoS_2$, with a Tafel slope of 44 mV/dec, displays slightly slower kinetics compared to $NiS_2$. The clustered micro-spherical morphology still provides a good density of active sites and structural porosity, which are advantageous. However, partial agglomeration may lead to reduced electrolyte diffusion to internal surfaces, slightly increasing resistance during the oxygen evolution process [70]. This explains why $CoS_2$ shows comparable but not superior kinetics compared to $NiS_2$.

FeS$_2$, on the other hand, shows the highest Tafel slope of 45 mV/dec, which aligns with its higher overpotential of 300 mV observed in **Figure 9(a).** This suggests slower reaction kinetics, due to its larger flake-like and blocky morphology, which limits the surface area and number of available active sites. Additionally, the relatively poor conductivity of FeS$_2$ compared to CoS$_2$ and NiS$_2$ may further contribute to the increased kinetic barrier [71].Tafel slope values in the range of 40-60 mV/dec typically suggest that the OER follows the adsorption–chemical step as the rate-determining step, and these results confirm that all three catalysts are operating within expected mechanistic pathways for metal sulfides in alkaline environments [72,73]. The slightly better kinetic performance of NiS$_2$ once again reinforces its potential as a promising, low-cost OER electrocatalyst.

**Figure 9(c)** shows a side-by-side comparison of overpotential and Tafel slope values for CoS$_2$, NiS$_2$, and FeS$_2$, giving a combined view of their OER activity. NiS$_2$ displays the best performance with the lowest overpotential of 260 mV and the smallest Tafel slope of 42 mV/dec, indicating that it requires less energy to start the oxygen evolution reaction and also proceeds faster once initiated. CoS$_2$ follows closely, with an overpotential of 270 mV and a Tafel slope of 44 mV/dec. Although slightly less efficient than NiS$_2$, it still shows good catalytic behavior. The moderate values suggest decent surface reactivity and reaction speed. FeS$_2$ shows the weakest performance, with the highest overpotential of 300 mV and Tafel slope of 45 mV/dec, suggesting it needs more energy to begin the reaction and has slower kinetics. This may be due to its less favorable morphology and lower conductivity.
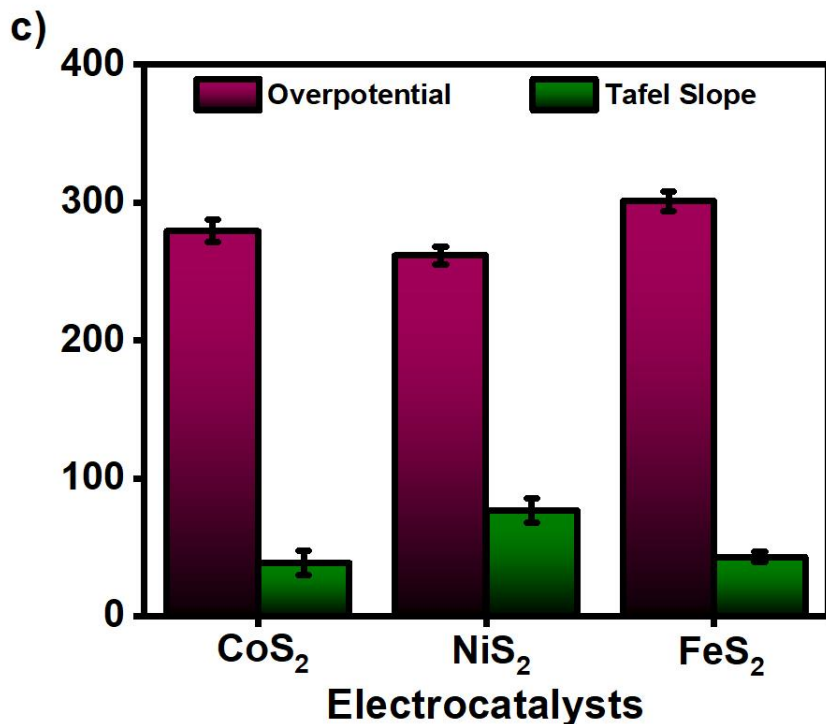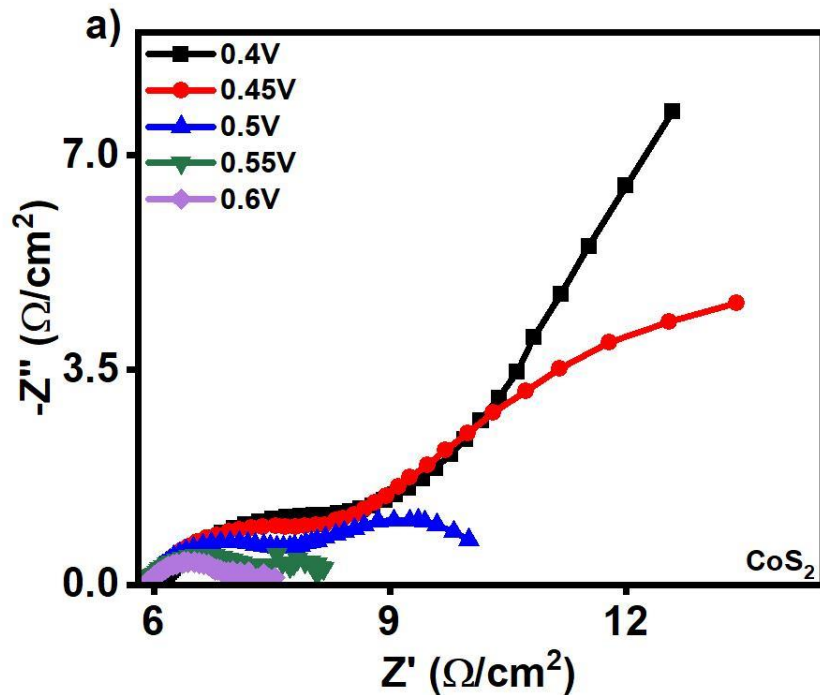
**Figure 9:** (a) OER polarization curve of $CoS_2$, $NiS_2$ and $FeS_2$; (b) tafel slopes; (c) comparison of tafel slope and overpotential.

Electrochemical impedance spectroscopy (EIS) was conducted to evaluate the charge transfer behavior and electrical conductivity of $CoS_2$, $NiS_2$, and $FeS_2$ electrocatalysts during the oxygen evolution reaction. The Nyquist plots in **Figure 10(a–c)** were recorded at different applied potentials ranging from 0.4 V to 0.6 V vs RHE. In these plots, a smaller semicircle corresponds to lower resistance and faster electron transfer, which directly supports higher catalytic activity. EIS is widely used to investigate such interfacial properties, especially for electrocatalysts involved in multi-electron reactions like OER [74,75]. Among the three, $NiS_2$ exhibits the smallest semicircle across the voltage range, indicating the lowest charge transfer resistance and most efficient electron mobility. This is consistent with its earlier electrochemical results, including the lowest overpotential (260 mV), smallest Tafel slope (42 mV/dec), and nanogranular

morphology observed in SEM, all of which contribute to its superior OER performance. $CoS_2$ shows moderate semicircle size, suggesting balanced charge transfer ability. This matches its overpotential of 270 mV, Tafel slope of 44 mV/dec, and its microsphere-like surface structure, which provides reasonable surface area and catalytic stability, though not as efficient as $NiS_2$ [76] . In contrast, $FeS_2$ displays the largest semicircle between 0.4 V and 0.6 V, reflecting higher resistance and slower charge movement at the electrode surface. These findings support its higher overpotential (300 mV), larger Tafel slope (45 mV/dec), and flake-like morphology, which likely limits active site exposure and hamper's reaction kinetics[77]. Overall, the EIS results within the 0.4-0.6 V range clearly support the previous LSV, Tafel, and SEM analyses, confirming that $NiS_2$ has the most favorably charged transport properties, followed by $CoS_2$ and $FeS_2$. This demonstrates the crucial role of morphology, conductivity, and interfacial charge transfer in determining OER efficiency in transition metal disulfide catalysts [78].
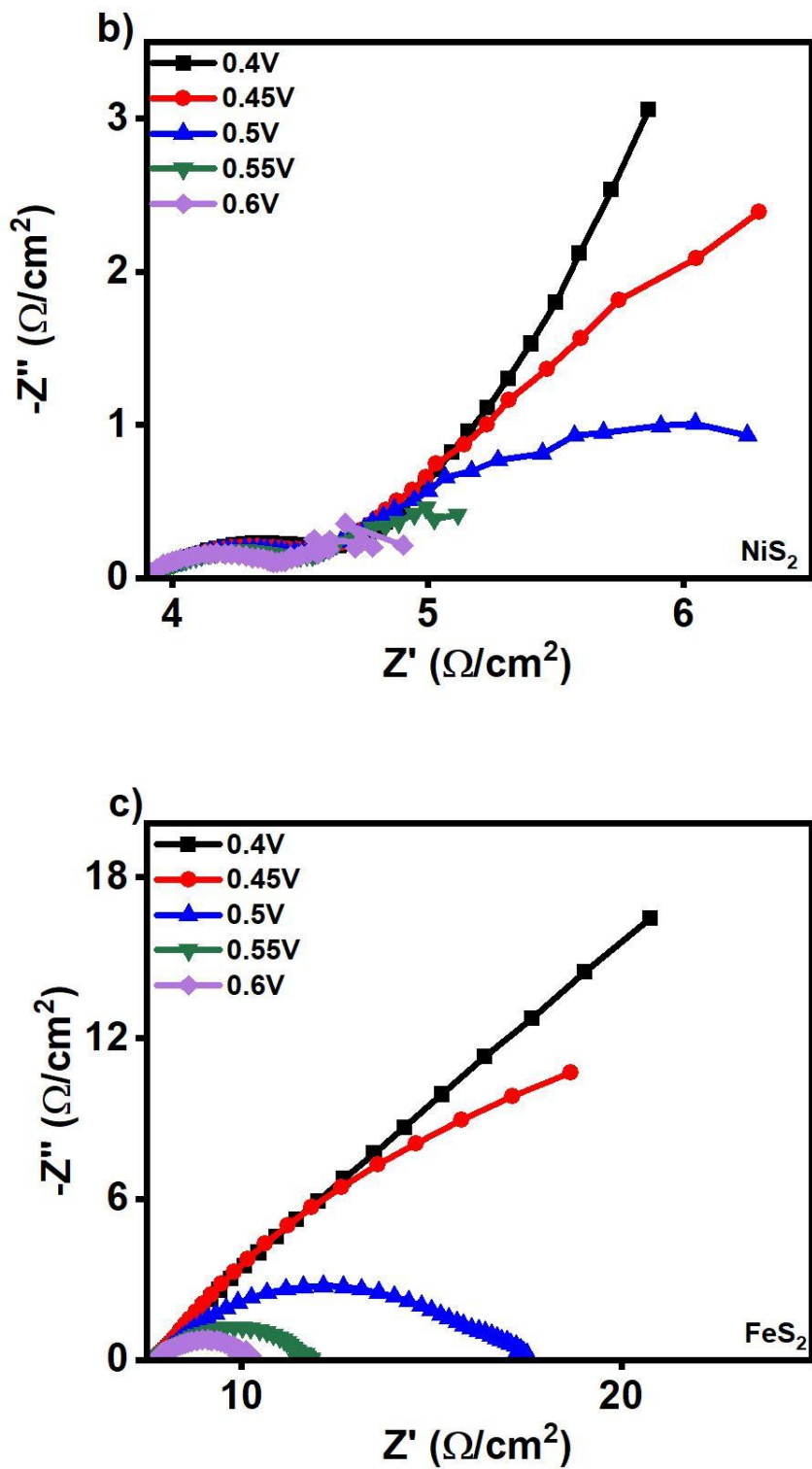
**Figure 10:** Nyquist plots for (a) $CoS_2$, (b) $NiS_2$ and (c) $FeS_2$

To better understand the catalytic behavior and availability of active sites on the synthesized $CoS_2$, $NiS_2$, and $FeS_2$ electrocatalysts, electrochemical double-layer capacitance ($C_{dl}$), electrochemical surface area (ECSA), and roughness factor (RF) were evaluated. These parameters are crucial to estimate how effectively a catalyst can engage in interfacial reactions and facilitate oxygen evolution under alkaline conditions [78,79]. The $C_{dl}$ values were calculated by performing cyclic voltammetry (CV) in the non-faradaic potential region at different scan rates, followed by plotting the current difference versus scan rate. The slope of the linear fit yields to the $C_{dl}$, based on **Equation (3.2)** where $I$ is the capacitive current and $v$ is the scan rate.

$I = vC_{dl}$.................................................................................................................(3.2)

As shown in **Figure 11(a)**, the estimated $C_{dl}$ values are 43.86mF/cm² for $NiS_2$ 9.18mF/cm² for $CoS_2$, and 6.85 mF/cm² for $FeS_2$. The significantly higher $C_{dl}$ of $NiS_2$ indicates greater surface interaction with electrolyte ions, reflecting more electrochemically accessible area, which directly contributes to better catalytic activity [80]. Using the calculated $C_{dl}$ values, the electrochemical surface area was derived using **Equation (3.3)** where $C_{dl}$ is the specific capacitance of a flat surface in 1 M KOH [81].
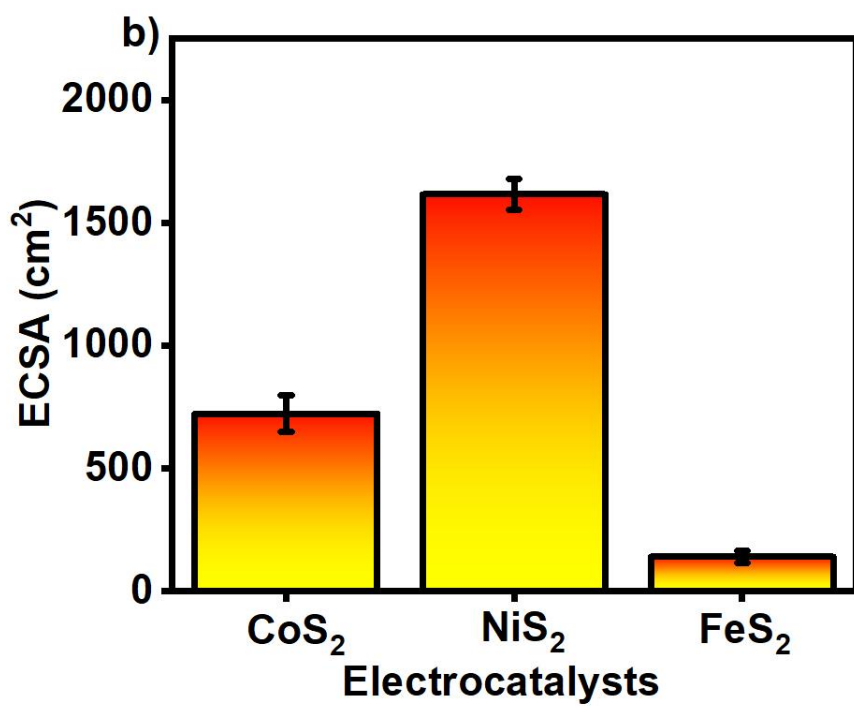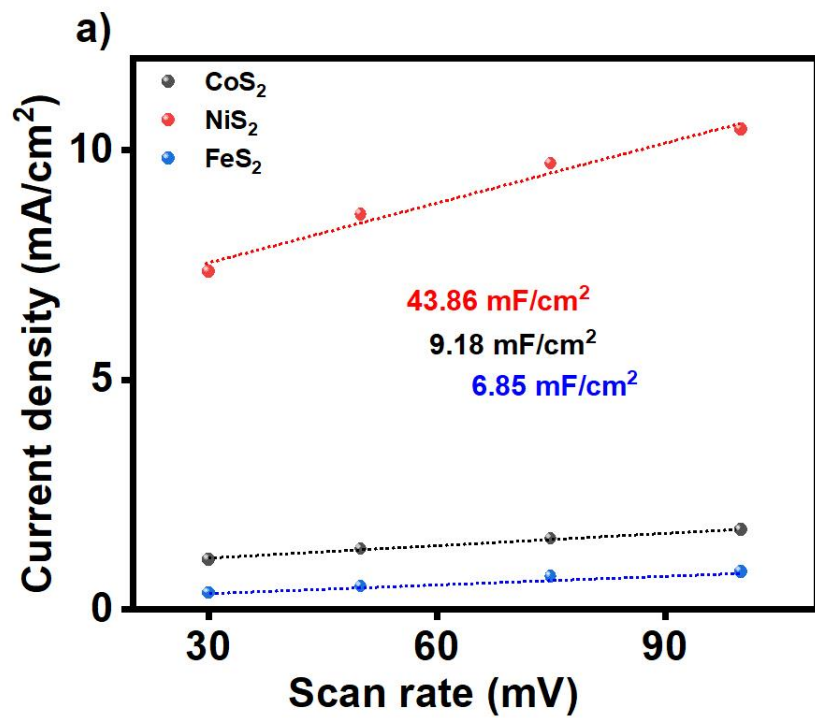
$ECSA = C_{dl}/C_s \; ; Cs = 0.04 \text{ mF/cm}^2$..........................................................................(3.3)

The resulting ECSA values are 1096 cm² for $NiS_2$, 229 cm² for $CoS_2$, and 171 cm² for $FeS_2$, as displayed in **Figure 11(b)**. These values clearly suggest that $NiS_2$ possesses a

larger ECSA compared to the other samples. This trend is consistent with earlier SEM results, where $NiS_2$ showed a uniform nanogranular structure, providing more active surface sites [82]. The high ECSA also correlates well with the superior OER performance of $NiS_2$ observed in **Figures 7(a–c)**, including its lowest overpotential and smallest Tafel slope.

To assess the texture and bubble-release ability of the catalyst surface, the roughness factor was computed using **Equation (3.4)** Here, GSA is the geometric surface area of the electrode.

$$RF = ECSA/GSA$$ .......................................................................................................(3.4)

The RF values were calculated to be 2000 for $NiS_2$, 344 for $CoS_2$, and 371 for $FeS_2$ **Figure 11(c).** A higher RF suggests a rougher and more porous surface, which is beneficial for efficient electrolyte diffusion, gas bubble evolution, and long-term catalytic durability [83]. $NiS_2$ has high RF confirms its good surface structure and supports the excellent performance observed in LSV and EIS. In summary, the $C_{dl}$, ECSA, and RF results collectively reinforce that $NiS_2$ has the most favorable surface characteristics, offering higher ion-accessibility, enhanced active site density, and optimized surface roughness. These properties contribute to its outstanding oxygen evolution efficiency. The lower values for $CoS_2$ and $FeS_2$ explain their comparatively moderate and lower OER performance. These findings further highlight the significance of nano structuring and surface engineering in designing high-performance, non-noble metal-based electrocatalysts for water splitting.
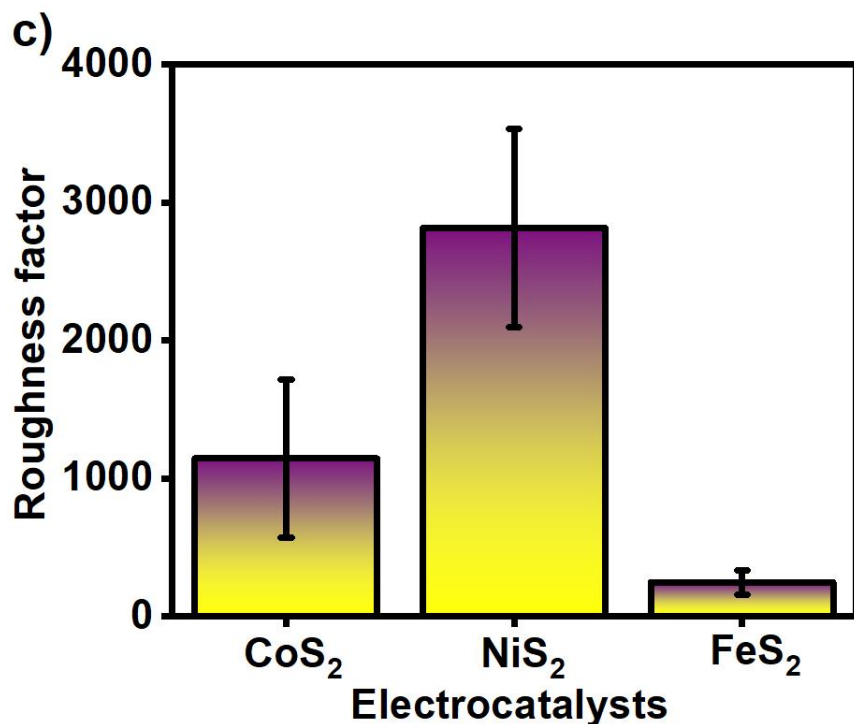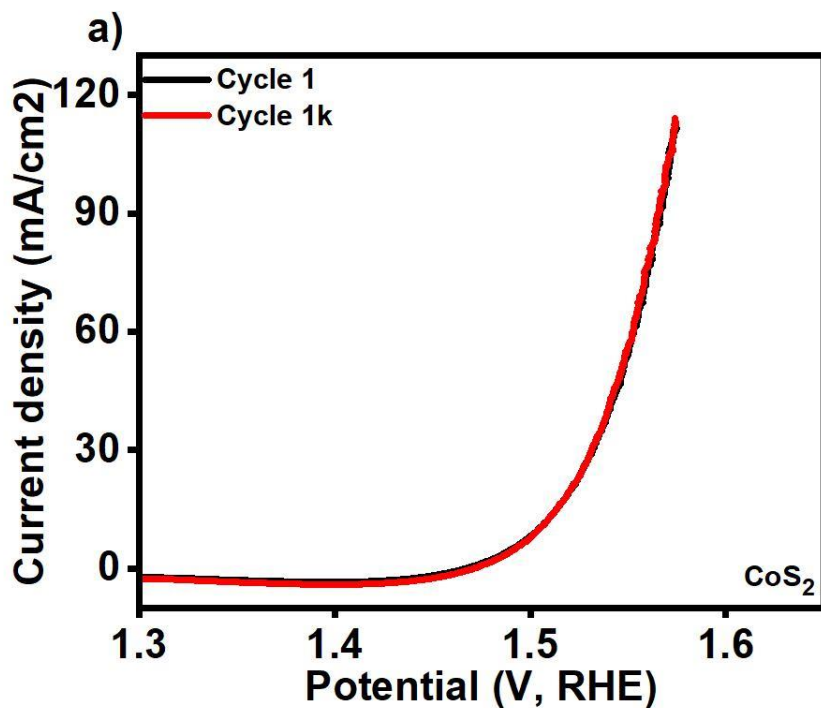
**Figure 11:** (a) Electrochemical double layer capacitance of $CoS_2$, $NiS_2$ and $FeS_2$ (b) electrochemical surface area, and (c) roughness factor of all as-synthesized samples.

The stability of electrocatalysts is a critical parameter that determines their long-term applicability in practical water-splitting systems. To assess the durability of the synthesized transition metal disulfides ($CoS_2$, $NiS_2$, and $FeS_2$), 1000 continuous LSV cycles were performed in 1 M KOH solution. The results are shown in **Figure 12(a-c)**, where the first and 1000th cycle polarization curves are overlaid for each sample. The minimal deviation observed between the first and last cycles for all three catalysts confirms their excellent electrochemical stability. This overlap indicates that the catalysts retained their structural integrity and active surface properties after extensive cycling. Among the three, $NiS_2$ and $CoS_2$ demonstrate especially consistent curves, suggesting highly robust and stable electrocatalytic behavior under prolonged operation. $NiS_2$, which earlier

exhibited the highest electrochemical surface area, lowest overpotential, smallest Tafel slope, and smallest charge transfer resistance, also shows outstanding cycling stability. This further supports its promise as a durable and high-performing OER catalyst. $CoS_2$ similarly maintains consistent activity after repeated use, which is attributed to its microstructure morphology and stable sulfide phase [84]. $FeS_2$, despite its lower overall OER performance, also maintains its polarization behavior over 1000 cycles without significant degradation. This suggests that while its surface activity is less pronounced compared to $NiS_2$, its structural stability in alkaline media is still noteworthy [85]. These results collectively highlight that all three catalysts exhibit excellent operational stability, an essential quality for long-term water-splitting applications. In particular, the combination of activity and durability positions $NiS_2$ as a highly promising candidate for scalable and sustainable electrochemical oxygen evolution.
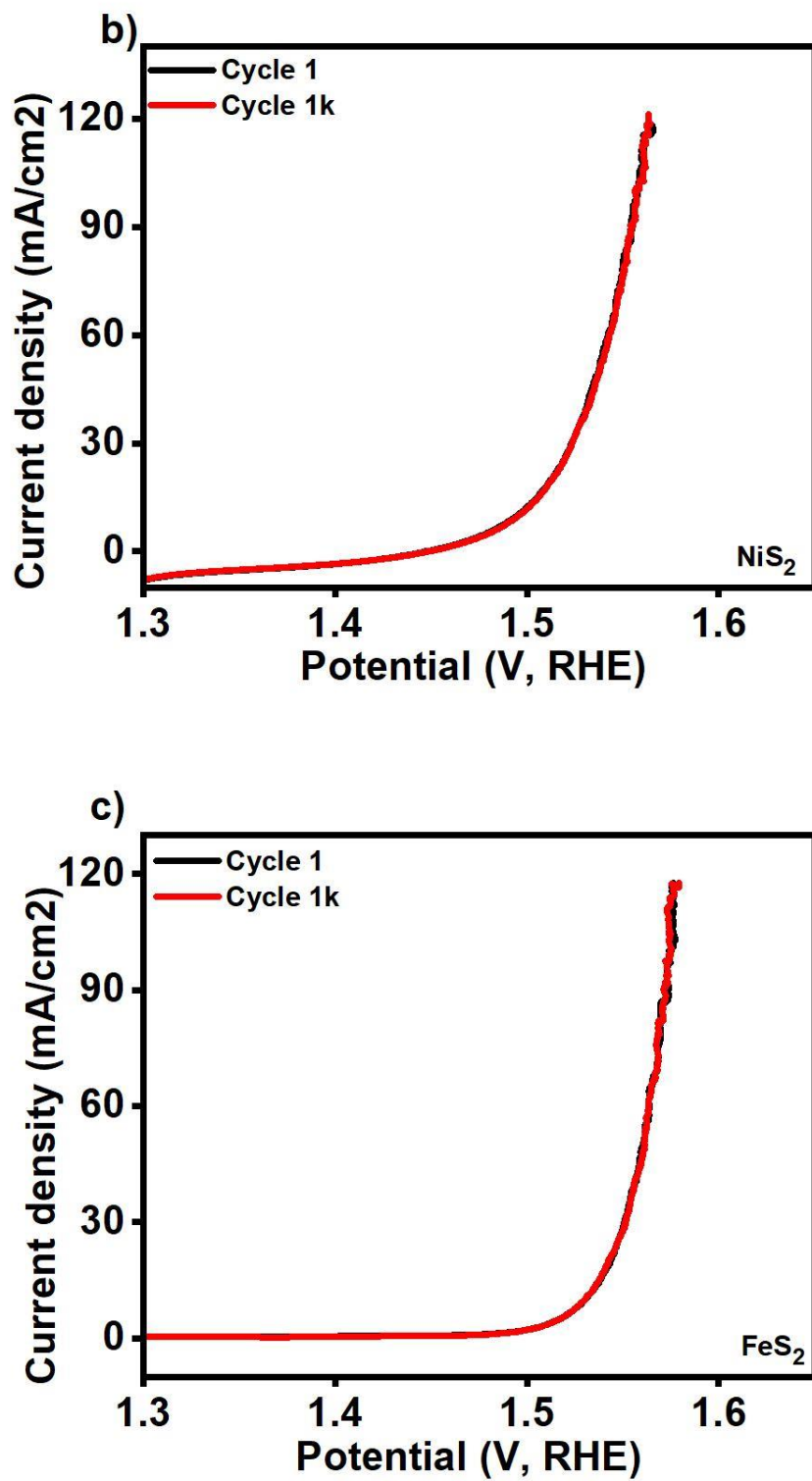
**Figure 12:** Polarization stability through 1000 cycles of LSV for (a) $CoS_2$, (b) $NiS_2$ and (c) $FeS_2$.

**Table 1.** Electrocatalytic activity of metal (Fe/Co/Ni) based materials towards OER.

| Material | Synthesis Method | Electrolyte | Overpotential (mV) | References |
|---|---|---|---|---|
| $FeS_2$/C | Microwave Heating | 1 M KOH | 240 @ 10 mA/cm² | [86] |
| $FeS_2$/C Nanowires | Microwave Heating | 1 M KOH | 291 @ 10 mA/cm² | [87] |
| $Co_8FeS_8$/CoS@CNT | Microwave-Assisted Bubble Bursting | 1 M KOH | 278 @ 10 mA/cm² | [88] |
| $NiS_2$/NiS/$Mn_2O_3$Nanofibers | Microwave-Assisted Synthesis | 1 M KOH | 333 @ 20 mA/cm² | [89] |
| $NiS_2$/$NiS_2$/NC | Microwave-Assisted Synthesis | 1 M KOH | 195 @ 10 mA/cm² | [90] |
| $NiS_2$ | Microwave-Assisted Synthesis | 1 M KOH | 380 @ 10 mA/cm² | [91] |
| $Fe_3S_4$ Nanosheets | Microwave-Assisted Synthesis | 1 M KOH | 230 @ 10 mA/cm² | [92] |
| $FeS_2$ | Microwave-Assisted Synthesis | 1 M KOH | 300 @ 10 mA/cm² | This work |
| $CoS_2$ | Microwave-Assisted Synthesis | 1 M KOH | 270 @ 10 mA/cm² | This work |
| $NiS_2$ | Microwave-Assisted Synthesis | 1 M KOH | 260 @ 10 mA/cm² | This work |

### 3.2.2. Hydrogen evolution reaction

Opposite to OER, or zero voltage with relation to the standard hydrogen electrode, is HER. That has faster kinetics than OER, mostly because it has fewer electrons and intermediate states with a lower thermodynamic barrier. A direct comparison of the HER electrocatalytic performance based on overpotential and Tafel slope is illustrated in **(Figure 13a, b)** for the microwave-synthesized $CoS_2$, $NiS_2$, and $FeS_2$ catalysts. These two parameters provide crucial insights into the thermodynamic efficiency and kinetic mechanisms of hydrogen evolution in alkaline media. $CoS_2$ demonstrated the lowest overpotential (240 mV) at 10 mA/cm² , followed by $NiS_2$ (244 mV) and $FeS_2$ (275 mV). A lower overpotential signifies more favorable energetics for HER. This superior performance of $CoS_2$ is strongly associated with its metallic conductivity, which enhances the availability of electrons at the catalyst electrolyte interface [93]. Additionally, $CoS_2$ possesses an optimal hydrogen binding energy close to zero, which ensures that hydrogen adsorption and desorption are energetically balanced, a key criterion for HER efficiency [94,95]. In contrast, $NiS_2$ showed a slightly higher overpotential than $CoS_2$, despite its high surface area and active site density. This suggests that, although $NiS_2$ offers abundant active sites, the intrinsic kinetics of HER may be limited due to its less favorable electronic structure compared to $CoS_2$ [96,97]. $FeS_2$, on the other hand, exhibited the highest overpotential, which aligns with its semiconducting nature that restricts charge transfer and results in poor catalytic activity in the absence of conductive modification.

As shown in **Figure 13(b)** The trend in Tafel slope $CoS_2$ (179 mV/dec) < $NiS_2$ (199 mV/dec) < $FeS_2$ (236 mV/dec) further supports the kinetic behavior of the catalysts. A lower Tafel slope suggests faster HER kinetics and a more efficient reaction pathway. The

Tafel slope values above 120 mV/dec indicate that the HER in these catalysts proceeds via the Volmer reaction (electrochemical hydrogen absorption) as the rate-determining step. $CoS_2$ has superior kinetic performance, which is linked to its high electronic conductivity and favorable surface energetics, which promote easier charge transfer and intermediate desorption [98]. $NiS_2$ has higher Tafel slope may be attributed to intermediate-strength hydrogen binding and higher charge transfer resistance, despite its nanostructured morphology [99]. The poorest kinetics in $FeS_2$ stem from its strong hydrogen adsorption energy and inefficient charge transport, which together slow down HER progress.
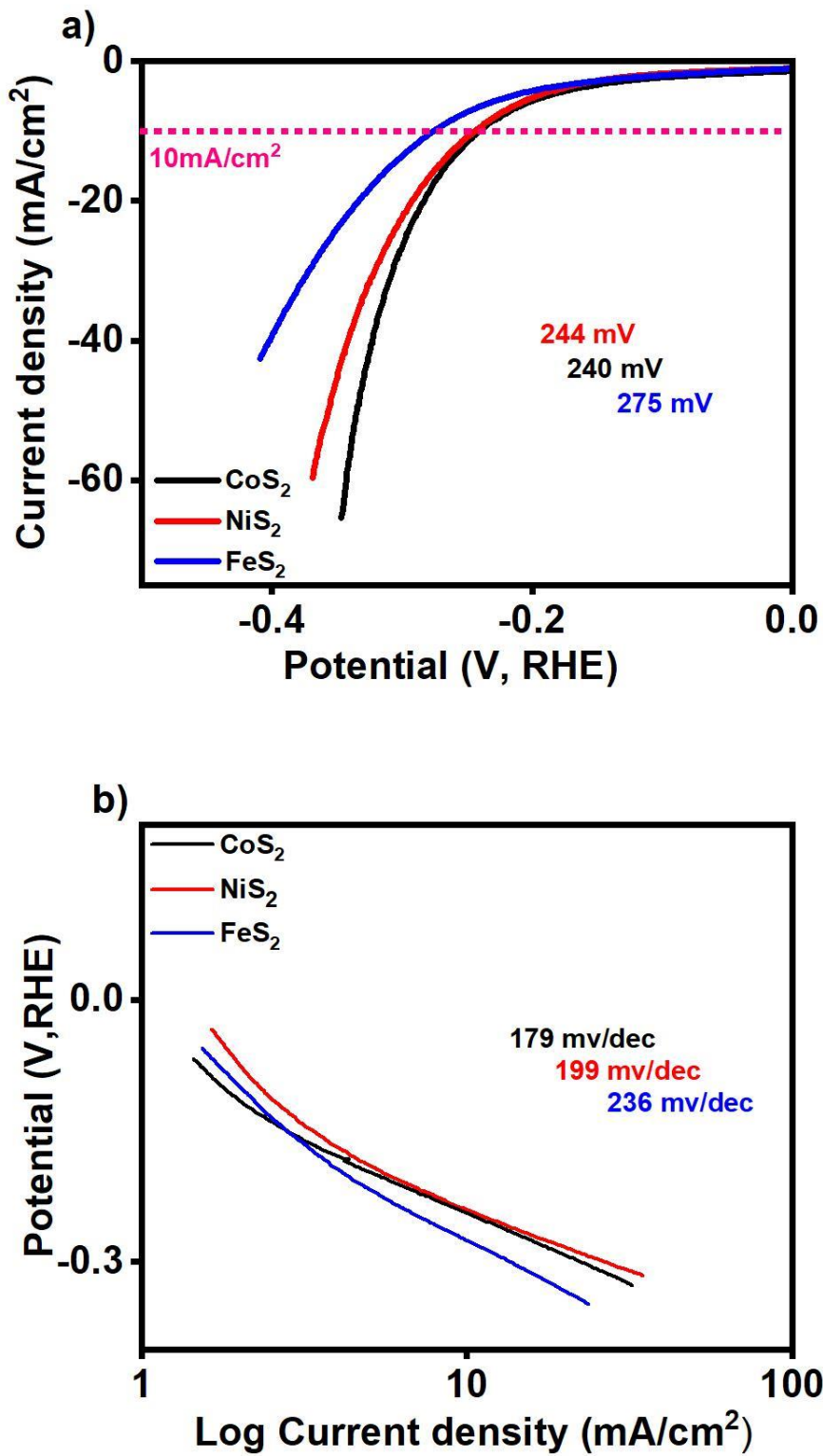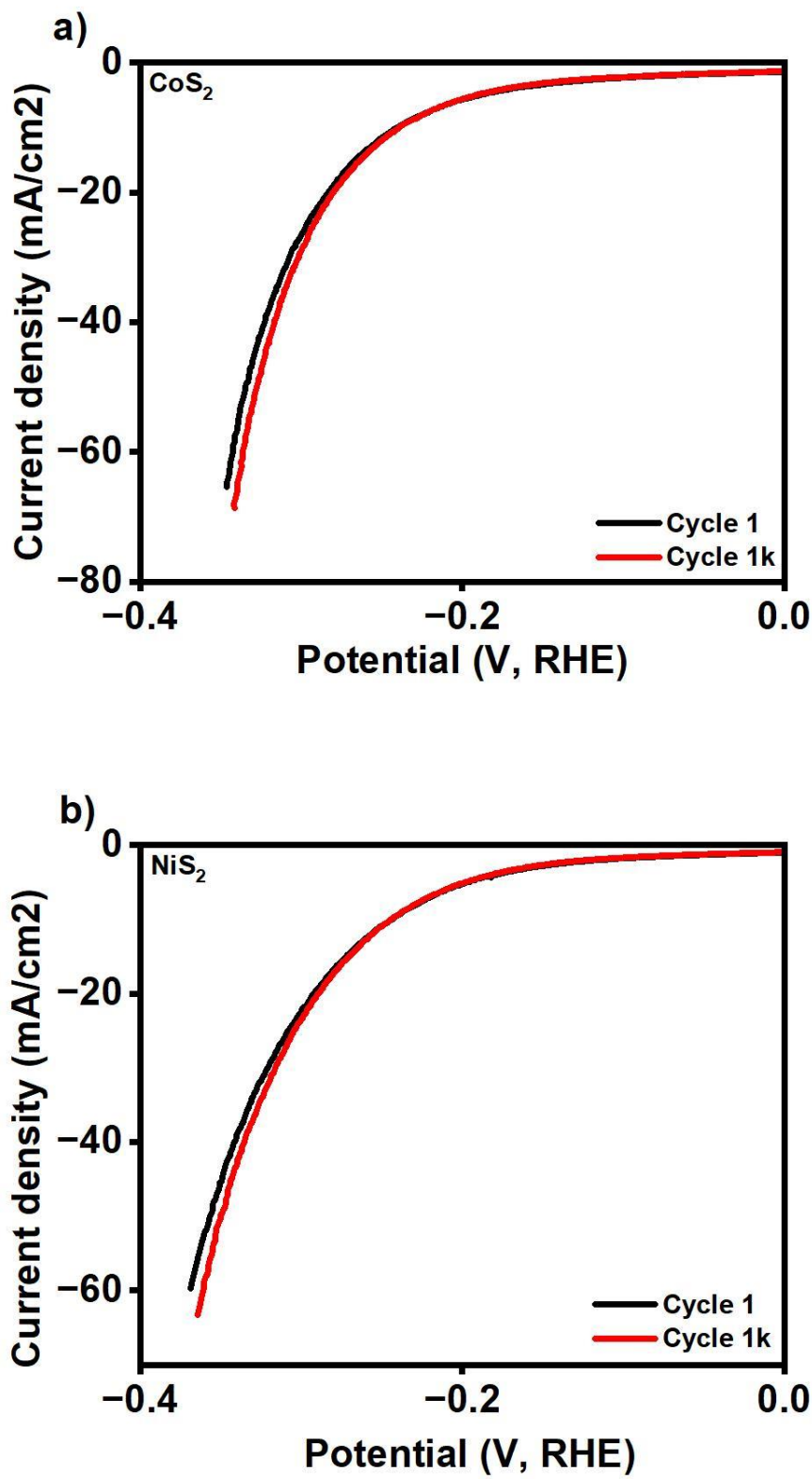
**Figure 13:** (a) HER polarization curve of $CoS_2$, $NiS_2$ and $FeS_2$, (b) tafel slopes

The electrochemical durability of an electrocatalyst is essential for long-term hydrogen production. To assess the HER stability of the microwave-synthesized samples, 1000 continuous LSV cycles were performed in 1 M KOH, as shown in **Figure 14(a–c).** The overlapping polarization curves between the initial (cycle 1) and final (cycle 1000) scans for $CoS_2$, $NiS_2$, and $FeS_2$ indicate that all three materials maintain their catalytic performance with minimal degradation. For $CoS_2$ **Figure 14(a)**, the negligible shift in the LSV curve confirms excellent structural and electrochemical stability, which is often attributed to its robust pyrite structure and metallic conductivity that resists surface passivation. Similarly, $NiS_2$ **Figure 14(b)** shows high retention of catalytic activity, due to partial surface oxidation forming a stable Ni-based hydroxide/sulfide shell that preserves HER kinetics during prolonged testing [100] . Despite having the lowest initial activity, $FeS_2$ **Figure 14(c)** also exhibits stable performance, suggesting its surface remains intact and chemically stable under alkaline cycling conditions.
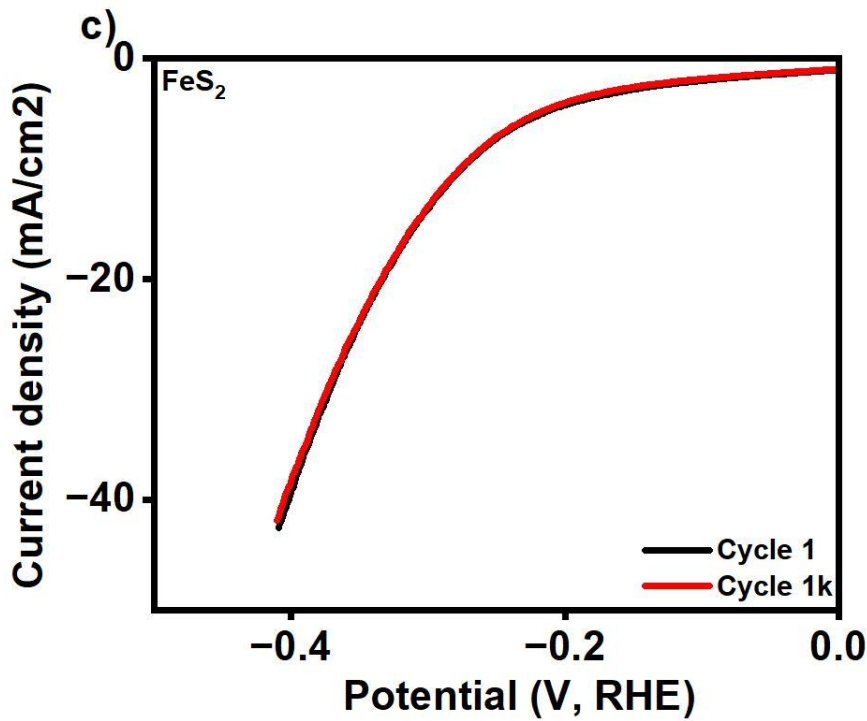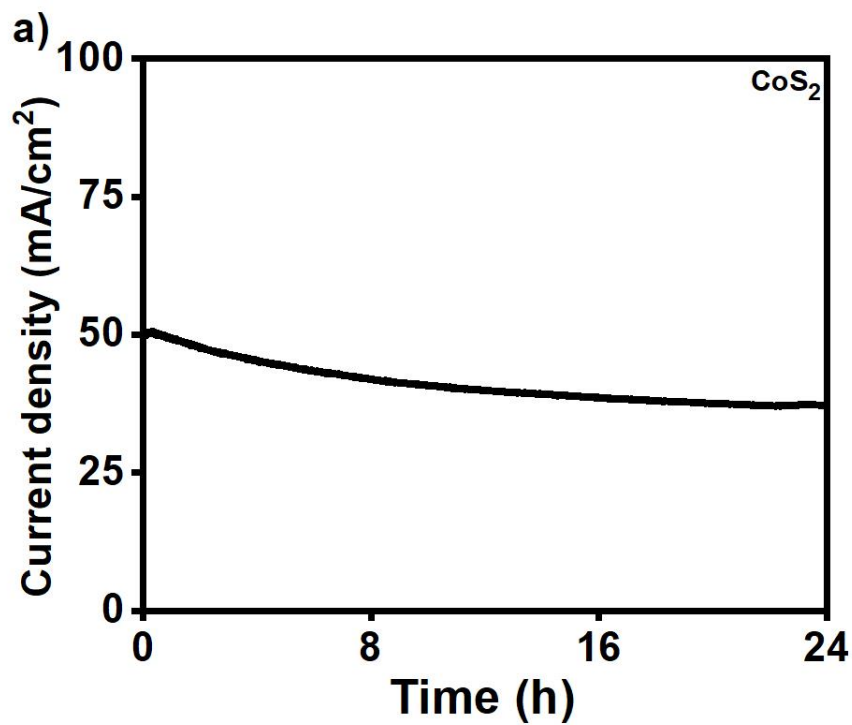
**Figure 14:** Polarization stability through 1000 cycles of LSV for (a) $CoS_2$, (b) $NiS_2$ and (c) $FeS_2$

To evaluate the long-term operational durability of the synthesized electrocatalysts, chronoamperometry (CA) tests were performed in 1 M KOH at a fixed potential for 24 hours, as shown in **Figure 15(a–c)**. Among the catalysts, $NiS_2$ exhibited the best retention in current density, maintaining values from 75 to 65 mA/cm² **(Figure 15b)**. The SEM images reveal a densely packed granular morphology, providing a continuous and compact network that supports efficient ironic and electronic transport. Moreover, its high electrochemical surface area and uniform Ni-S distribution **(Figure 7c)** further contribute to its extended catalytic stability, in line with previously reported Ni-based disulfide morphologies known for enhancing HER durability [74]. $CoS_2$ showed moderate stability, with current density decreasing from 50 to 38 mA/cm² over 24 hours **(Figure 15a)**. The SEM images **(Figure 6a, b)** depict aggregated, cauliflower-like spherical particles that

offer increased active surface area and mechanical cohesion. Such structures have been reported to improve electrocatalytic robustness under prolonged testing. The EDX mapping **(Figure 6c)** confirms uniform Co and S distribution, ensuring sustained active sites; however, the less compact nature compared to $NiS_2$ might result in structural weakening over time. $FeS_2$ retained current from 43 to 33 mA/cm² **(Figure 15c)**, indicating lower but acceptable stability. SEM micrographs **(Figure 8a, b)** show irregular, plate-like layered structures, which, while structurally broad, may hinder efficient charge movement. EDX mapping **(Figure 8c)** displays fairly uniform Fe and S elemental dispersion, but the lower ECSA and higher charge transfer resistance limit electron accessibility and catalytic longevity. Similar durability limitations of $FeS_2$ due to its structural and kinetic constraints have been observed previously.
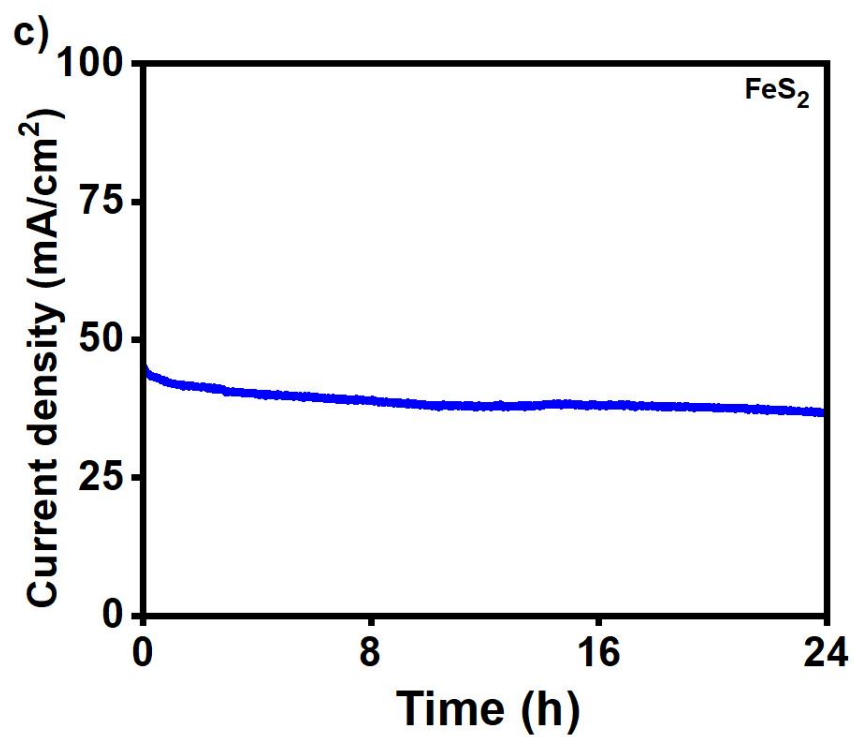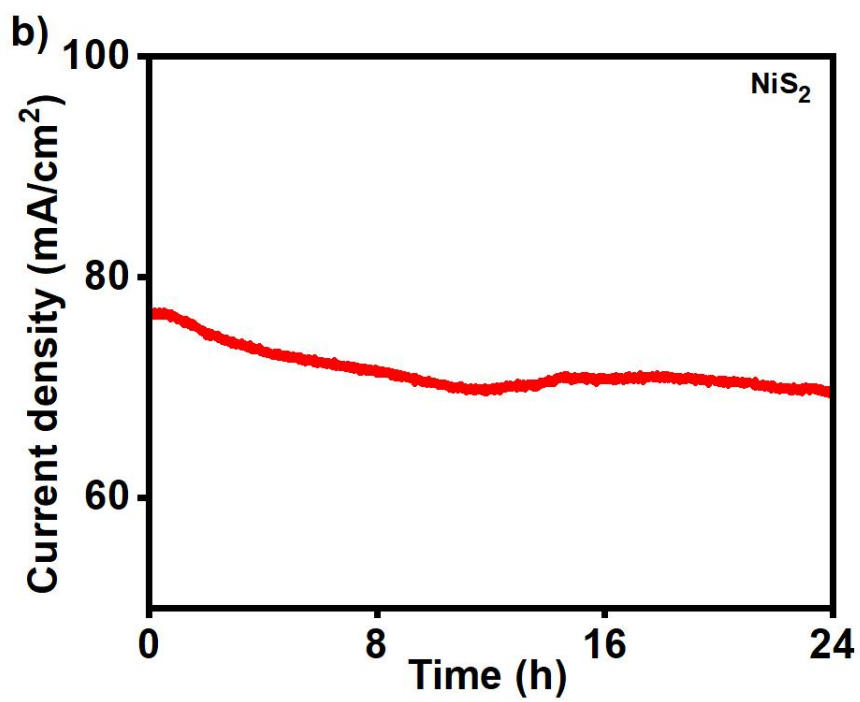
**Figure 15:** Chronoamperometry test for the water splitting process for 24h for the (a) $CoS_2$, (b) $NiS_2$ and (c) $FeS_2$.

**Table 2.** Electrocatalytic activity of metal (Fe/Ni/Co) based materials towards HER.

| Material | Synthesis Method | Electrolyte | Overpotential @ 10 mA/cm² (mV) | Reference |
|---|---|---|---|---|
| NiS$_2$ Nanocubes | Microwave-assisted | 1 M KOH | 248 | [101] |
| CoS$_2$ Hollow Nano boxes | Microwave-assisted | 1 M KOH | 230 | [102] |
| FeS$_2$ Microspheres | Microwave-assisted | 1 M KOH | 265 | [103] |
| FeS$_2$ | Microwave-assisted | 1 M KOH | 255 | [104] |
| Ni$_3$S$_4$/NiS$_2$/FeS$_2$ | Microwave-assisted | 1 M KOH | 226 | [104] |
| CoS$_2$ | Microwave-assisted | 1 M KOH | 240 | This work |
| NiS$_2$ | Microwave-assisted | 1 M KOH | 244 | This work |
| FeS$_2$ | Microwave-assisted | 1 M KOH | 275 | This work |
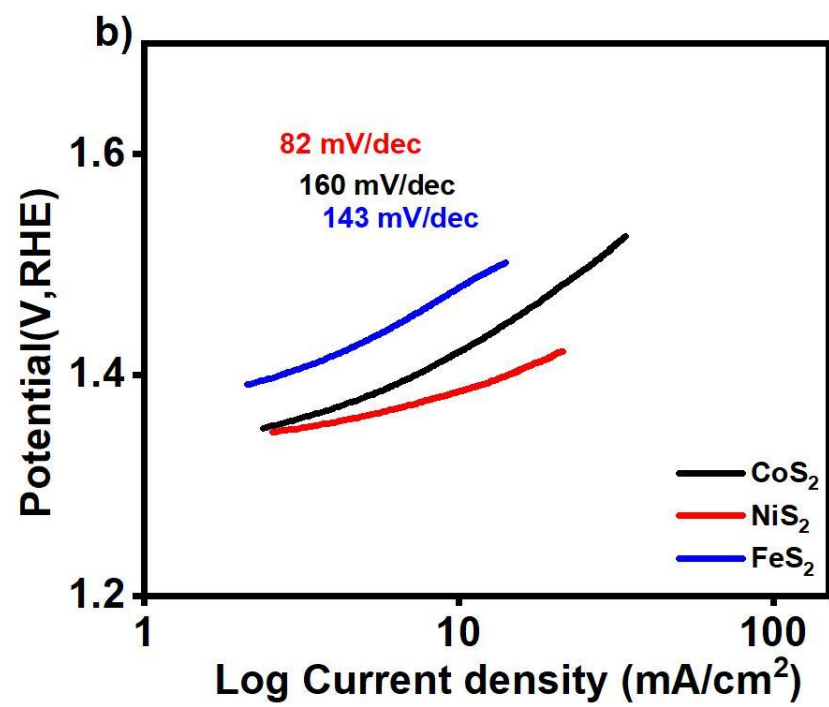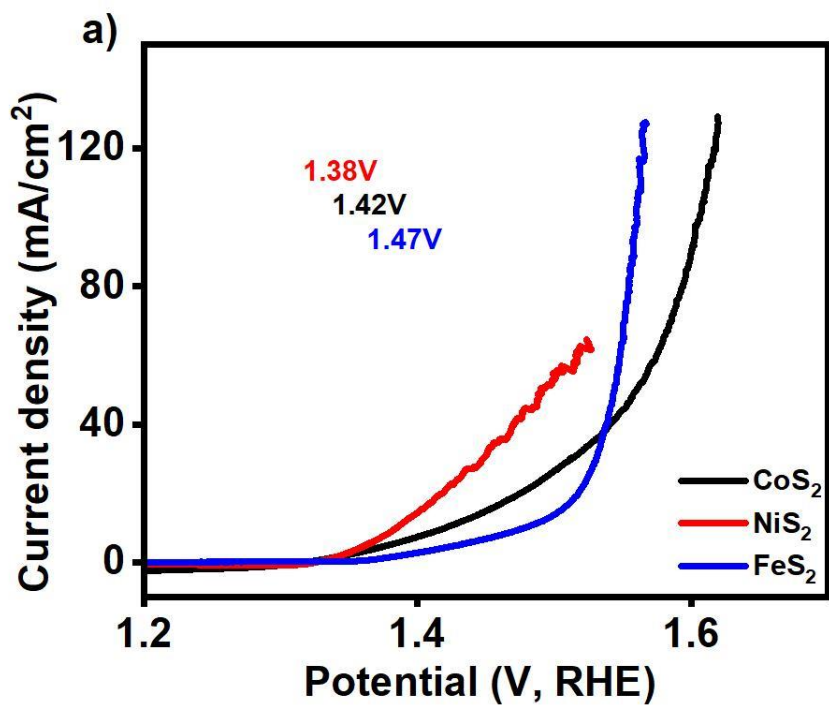
### 3.2.3. Urea oxidation reaction
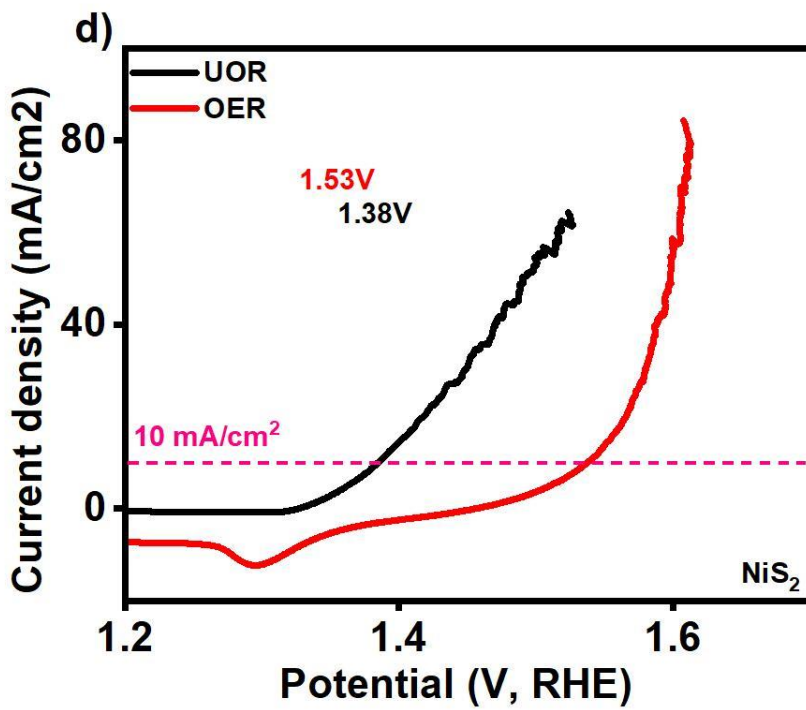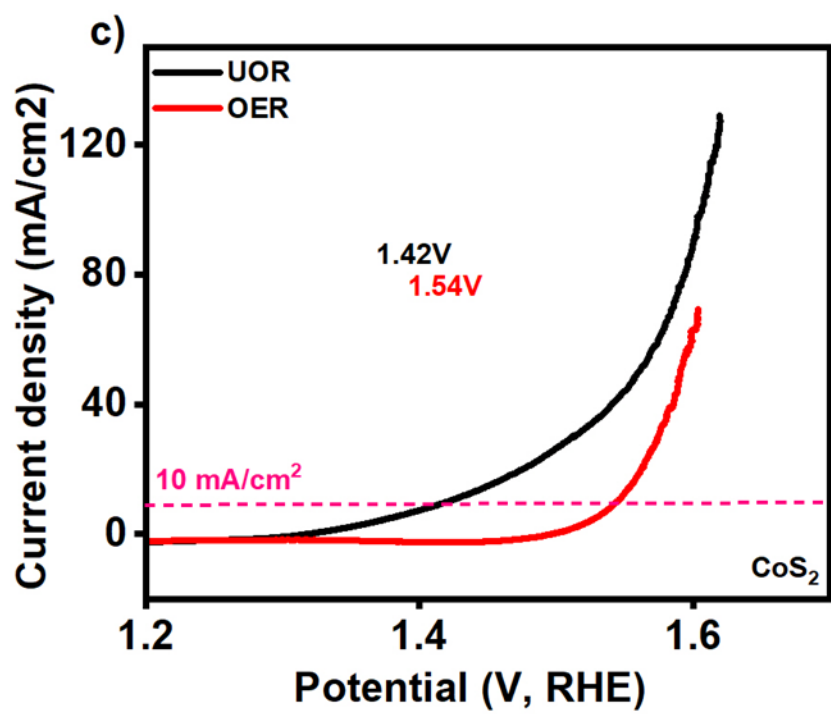
Upon the introduction of 0.33 M urea into the 1 M KOH electrolyte, the electrocatalytic performance of the synthesized metal sulfides CoS$_2$, NiS$_2$, and FeS$_2$ toward the urea oxidation reaction was significantly enhanced, as evidenced by their low onset potential. UOR serves as an energy-efficient alternative to the conventional OER. Additionally, UOR facilitates the treatment of urea-rich wastewater by converting urea into harmless nitrogen and carbon dioxide gases, offering dual benefits in energy generation and environmental remediation[105]. The UOR activities of CoS$_2$, NiS$_2$, and FeS$_2$ were evaluated, as depicted in **Figure 16(a)**. Among these, NiS$_2$ exhibited the lowest onset potential of 1.35 V at a current density of 10 mA/cm², outperforming CoS$_2$ and FeS$_2$, which

displayed onset potentials of 1.42 V and 1.47 V, respectively. The superior performance of $NiS_2$ can be attributed to its favorable electronic structure and the presence of active $Ni^{2+}/Ni^{3+}$ redox couples, which enhance the adsorption and oxidation of urea molecules [106]. $CoS_2$ also demonstrated commendable activity, likely due to its nanostructured morphology and the redox versatility of $Co^{2+}/Co^{3+}$ species, which facilitate efficient charge transfer during the oxidation process [107]. In contrast, $FeS_2$ showed the highest onset potential among the three, suggesting that higher overpotentials are required to initiate the reaction, possibly due to less favorable electronic properties and fewer active sites for urea adsorption and oxidation. To further investigate the reaction kinetics, Tafel slope analysis was conducted, as shown in **Figure 16(b)**. $NiS_2$ displayed the lowest Tafel slope of 87.7 mV/dec, indicating more favorable kinetics for UOR. $CoS_2$ and $FeS_2$ exhibited higher Tafel slopes of 160 mV/dec and 143 mV/dec, respectively, suggesting slower electron transfer rates and less efficient catalytic processes. The higher Tafel slope observed for $FeS_2$ reinforces its sluggish catalytic behavior in UOR, which may be attributed to its limited conductivity and lower intrinsic activity of iron sites under alkaline conditions. These trends correlate well with the observed SEM morphologies, where $NiS_2$ possesses a dense, interconnected structure conducive to enhanced urea diffusion and electron transport. In summary, $NiS_2$ outperforms both $CoS_2$ and $FeS_2$ in terms of onset potential and reaction kinetics, establishing it as the most efficient electrocatalyst among the tested materials for UOR in alkaline medium. These findings are consistent with recent studies highlighting the promising role of nickel-based sulfides in energy-efficient and environmentally friendly urea-assisted hydrogen generation systems.

To investigate the bifunctional electrocatalytic performance of the synthesized metal disulfides ($CoS_2$, $NiS_2$, and $FeS_2$), their activity toward both the urea oxidation reaction and the oxygen evolution reaction was systematically evaluated in 1 M KOH solution. Among the tested catalysts, $NiS_2$ exhibited the lowest onset potential for UOR (1.38 V vs. RHE) and achieved a current density of 10 mA/cm² at this potential, outperforming $CoS_2$ (1.42 V) and $FeS_2$ (1.47 V), as shown in **Figure 16(c-f)**. This outstanding UOR performance of $NiS_2$ can be attributed to its high electrical conductivity and favorable electronic configuration, which enable efficient adsorption and activation of urea molecules and intermediates [108]. Moreover, nickel-based sulfides are known to undergo surface reconstruction under alkaline electrochemical conditions, forming active Ni $(OH)_2$/NiOOH species that accelerate urea electrooxidation via a multi-step dehydrogenation mechanism [109]. This surface transformation provides more catalytically active sites for the cleavage of N–H and C–N bonds in urea, thereby lowering the energy barrier for the reaction [110]. In comparison, $CoS_2$ showed slightly higher UOR onset potential (1.42 V), but its performance remained competitive due to the possible in situ formation of CoOOH or $CoO_x$ species, which can facilitate electrochemical oxidation through similar reconstruction-driven mechanisms [111]. However, $FeS_2$ demonstrated the poorest UOR performance with an onset potential of 1.47 V, which may be attributed to its lower conductivity, fewer active sites, and limited surface reconstruction dynamics [112]. Previous reports have indicated that iron sulfides often suffer from weak adsorption of urea-derived intermediates and lower charge-transfer efficiency, which hinders their catalytic efficiency. When comparing the UOR and OER performances, all three catalysts required lower overpotentials for UOR than for OER, confirming the thermodynamic

advantage of using urea as an anodic feedstock. As shown in **Figure 16(c–e)**, NiS$_2$ showed a significantly lower onset potential for UOR (1.38 V) compared to OER (1.53 V), illustrating its energetic favorability for replacing OER in water splitting. CoS$_2$ followed a similar trend (UOR: 1.42 V vs. OER: 1.54 V), while FeS$_2$ exhibited the smallest difference (UOR: 1.47 V vs. OER: 1.55 V), reinforcing the observation that NiS$_2$ is more suitable for low-energy urea-assisted electrolysis. The higher current densities observed in UOR for all materials suggest faster reaction kinetics than OER, as the cleavage of C-N and N-H bonds in urea proceeds with a lower thermodynamic barrier than the O-O bond formation in OER. These results collectively highlight NiS$_2$ as the most promising bifunctional catalyst, demonstrating superior activity for both UOR and OER. Its dual-functionality makes it particularly valuable for integrated electrochemical systems aimed at sustainable hydrogen production via urea-assisted water splitting, enabling lower energy consumption and wastewater treatment simultaneously.

c)

**CoS₂**

d)
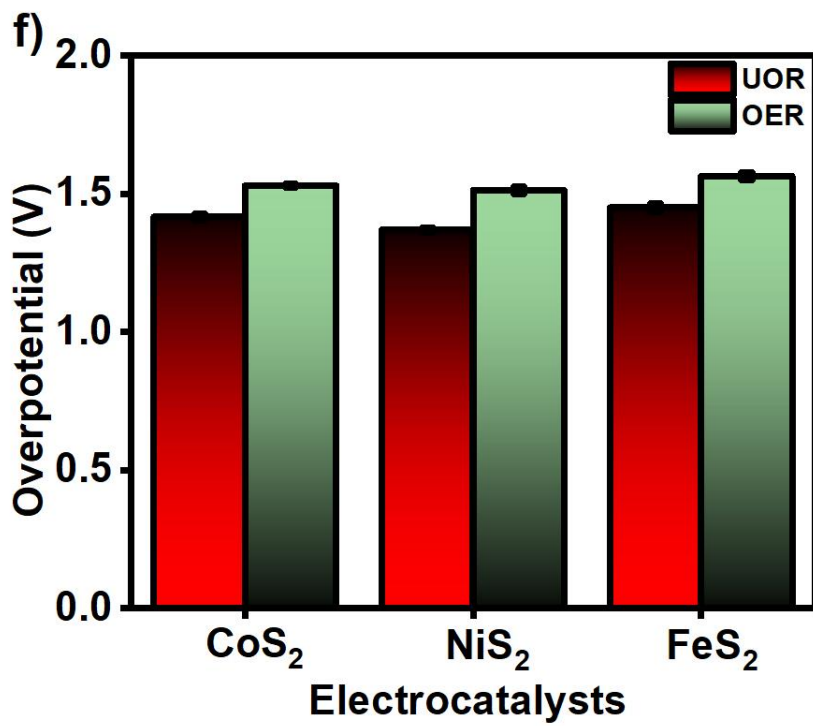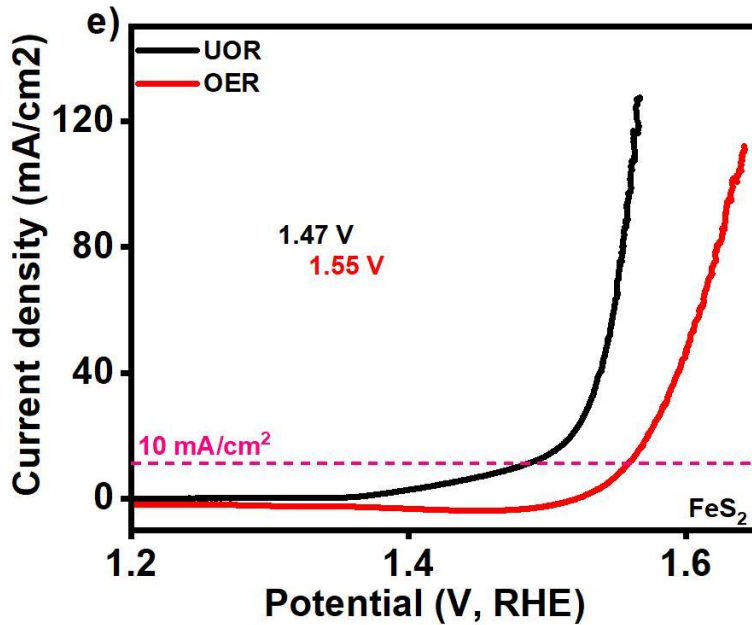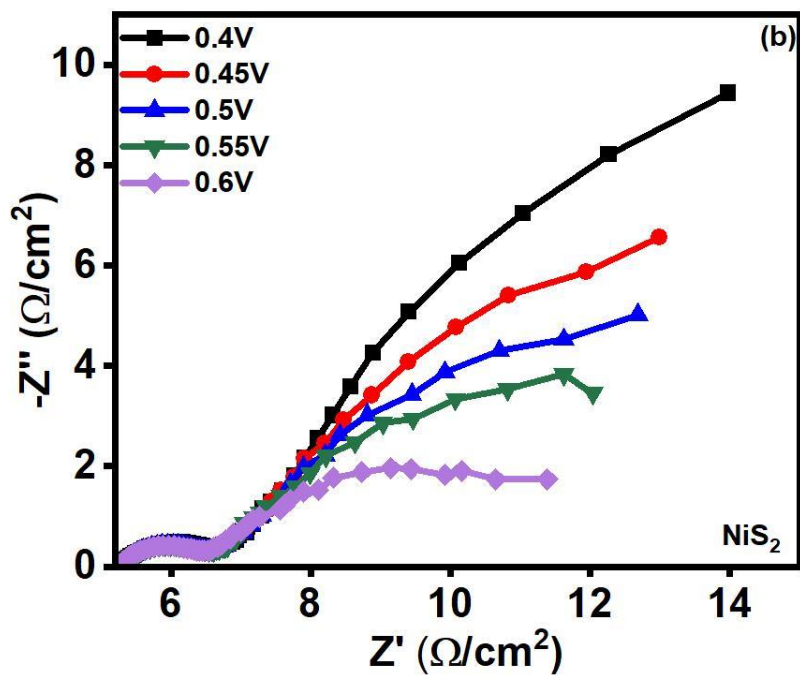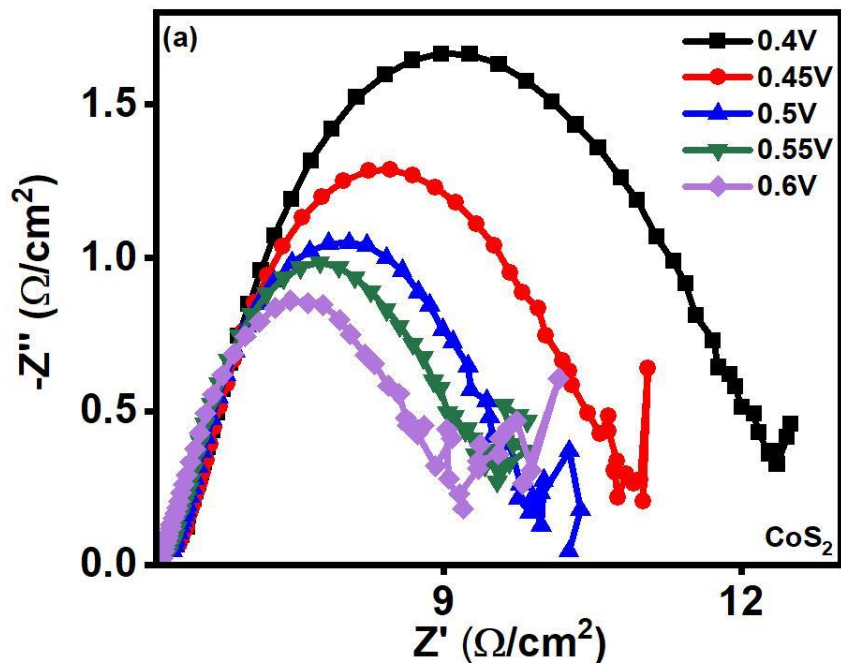
**NiS₂**

**Figure 16:** Electrocatalytic performance for UOR: (a) LSV curves of CoS₂, NiS₂, and FeS₂ catalysts applied for electrochemical UOR (0.33 M urea in 1 M KOH), (b)Tafel slope (c-e) comparison of onset potential of the OER and UOR at 10 mA/cm² for CoS₂, NiS₂, and FeS₂.

Electrochemical impedance spectroscopy was performed to elucidate the interfacial charge transport kinetics of the synthesized transition metal disulfides ($CoS_2$, $NiS_2$, and $FeS_2$) under urea oxidation reaction conditions in 1 M KOH+0.3M Urea. The Nyquist plots obtained at various potentials from 0.4 V to 0.6 V vs. RHE are presented in **Figure 17(a-c)**, and the charge transfer resistance $R_ct$ values were estimated at 0.6 V from the diameter of the high-frequency semicircle. The calculated $R_ct$ values were 1.1 $\Omega$ for $NiS_2$, 2.6 $\Omega$ for $CoS_2$, and 4.0 $\Omega$ for $FeS_2$, revealing a clear hierarchy in interfacial electron transfer performance. The lowest $R_{ct}$ observed for $NiS_2$ confirms its superior conductivity and faster charge transport during UOR, which directly correlates with its best catalytic performance lowest onset potential (1.38 V) and highest current density at 10 mA/cm² as shown in **Figure 16(d and f)**. This enhanced behavior can be attributed to the favorable surface activation of $NiS_2$ into NiOOH species, along with abundant active sites and low electron transfer barriers [113]. Although $CoS_2$ exhibits a slightly higher $R_ct$ (2.6 $\Omega$), it still demonstrates decent catalytic efficiency **Figure 16(c and f)** due to its intrinsic metallicity and in situ oxidation into active CoOOH layers. In sharp contrast, $FeS_2$ presents a significantly larger $R_ct$ of 4.0 $\Omega$, indicating sluggish charge transfer and poor interfacial electron mobility. This is consistent with its weak UOR performance (onset to potential 1.47 V, lowest current density; **Figure 16(e and f)**, and can be linked to poor conductivity, limited surface reconstruction, and low active site exposure. The EIS results therefore prove that $NiS_2$ is the most efficient catalyst in terms of charge transfer, followed by $CoS_2$, while $FeS_2$ performs the worst among the three. These findings, in conjunction with the LSV results from **Figure 16(a–f)**, confirm that the excellent UOR activity of $NiS_2$ arises not only from high intrinsic catalytic activity but also from superior interfacial charge

transport properties making it a promising candidate for low-energy, urea-assisted hydrogen production.
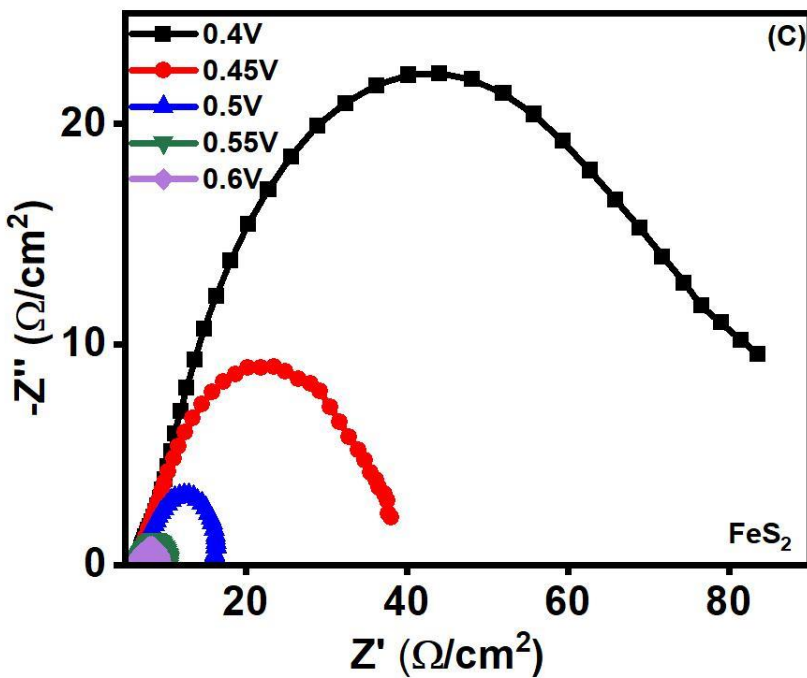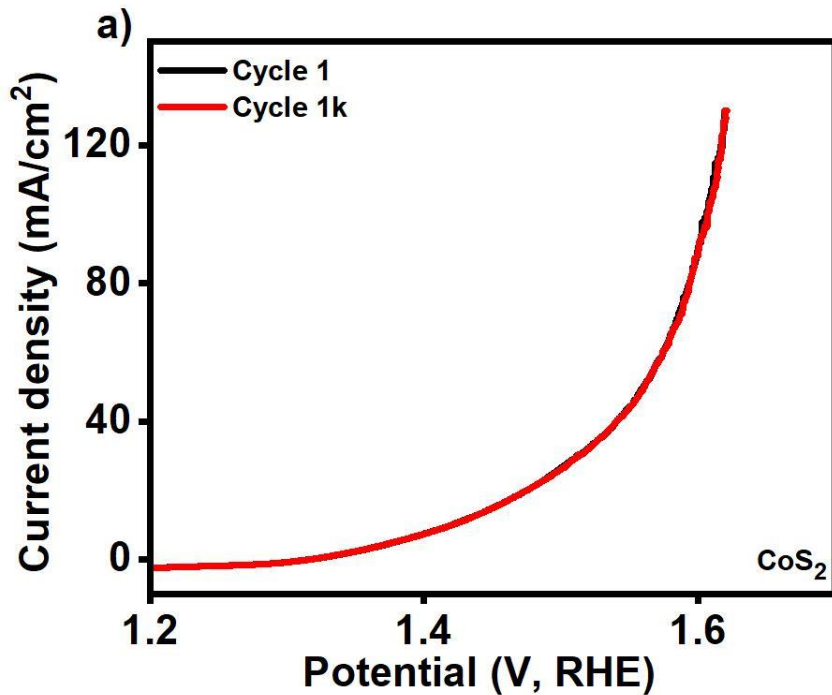
**Figure 17:** Nyquist plots for (a) $CoS_2$, (b) $NiS_2$, and (c) $FeS_2$

The electrochemical stability of the synthesized $CoS_2$, $NiS_2$, and $FeS_2$ electrocatalysts toward the urea oxidation reaction was evaluated through continuous cyclic voltammetry testing over 1000 cycles in 1 M KOH containing urea. The linear sweep voltammetry curves before and after cycling are presented in **Figure 18(a–c)**. All three catalysts demonstrated excellent durability, as evidenced by the minimal change in current density between the initial (Cycle 1) and final (Cycle 1000) LSV curves. In the case of $CoS_2$ **Figure 18(a)**, the overlap of the curves indicates exceptional electrochemical robustness and structural integrity under prolonged operation. $FeS_2$ **(Figure 18c)** also showed identical LSV profiles before and after cycling, confirming its long-term stability during UOR. $NiS_2$ (**Figure 18b**) displayed a slight decrease in current density after 1000 cycles, particularly at higher potential, which may be due to minor surface changes or

partial passivation of active sites. Nevertheless, the change was minimal, and overall stability remained high. These results confirm that all three metal disulfide electrocatalysts possess good electrochemical durability for UOR, with $CoS_2$ and $FeS_2$ maintaining highly stable performance, and $NiS_2$ showing only a slight decline after extended cycling.
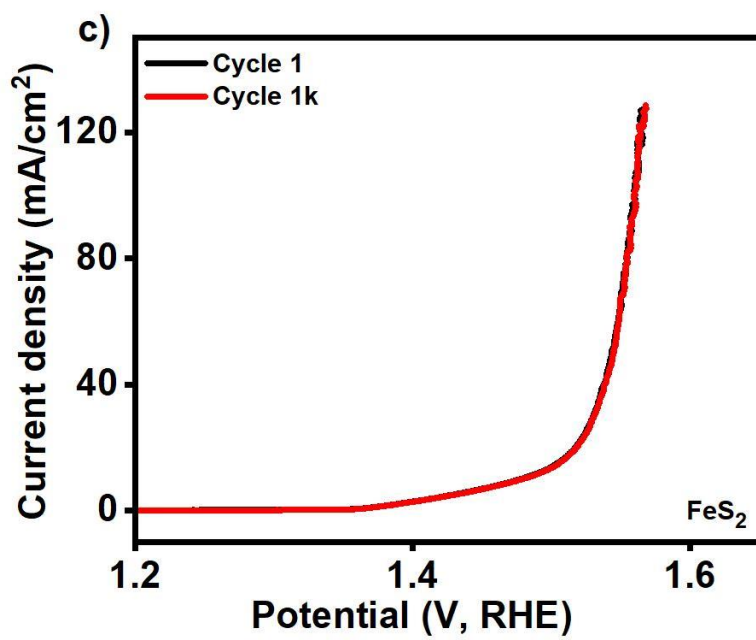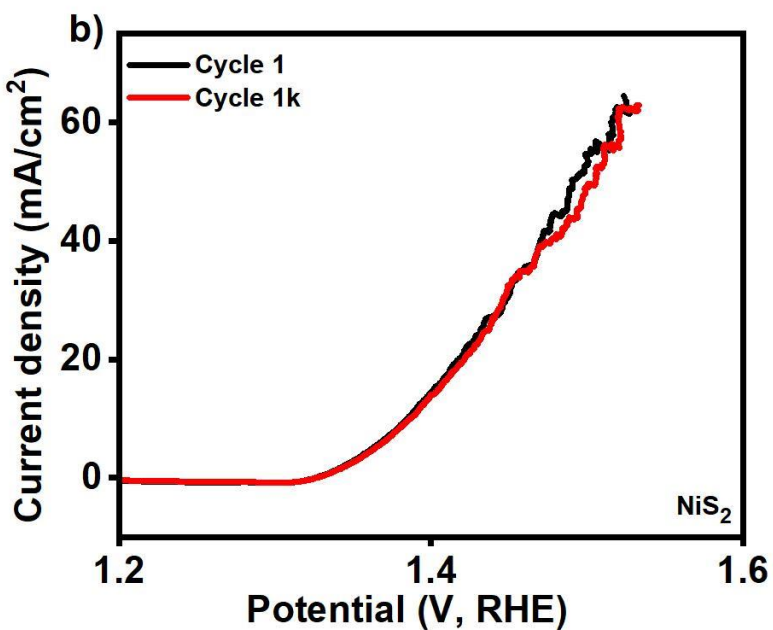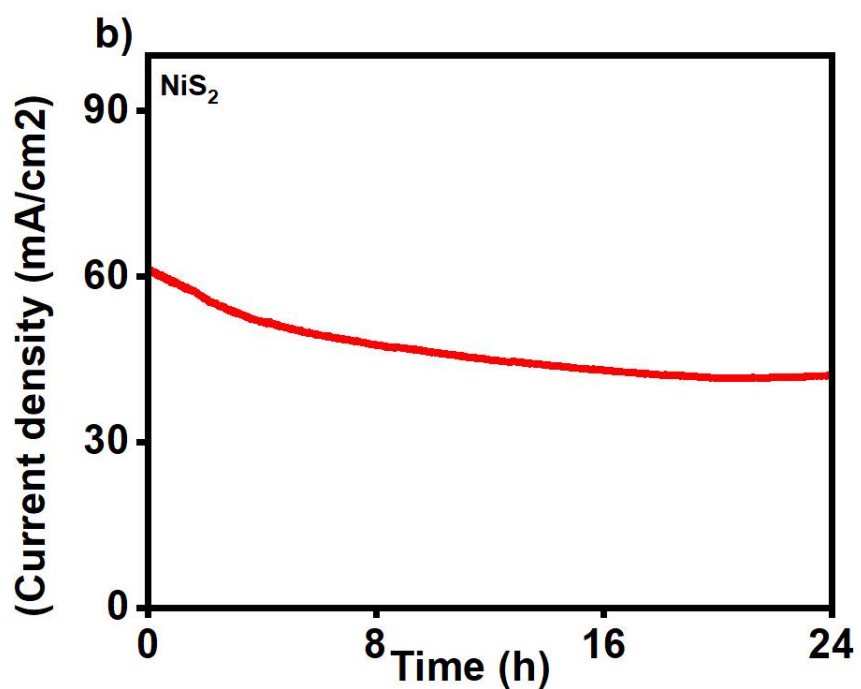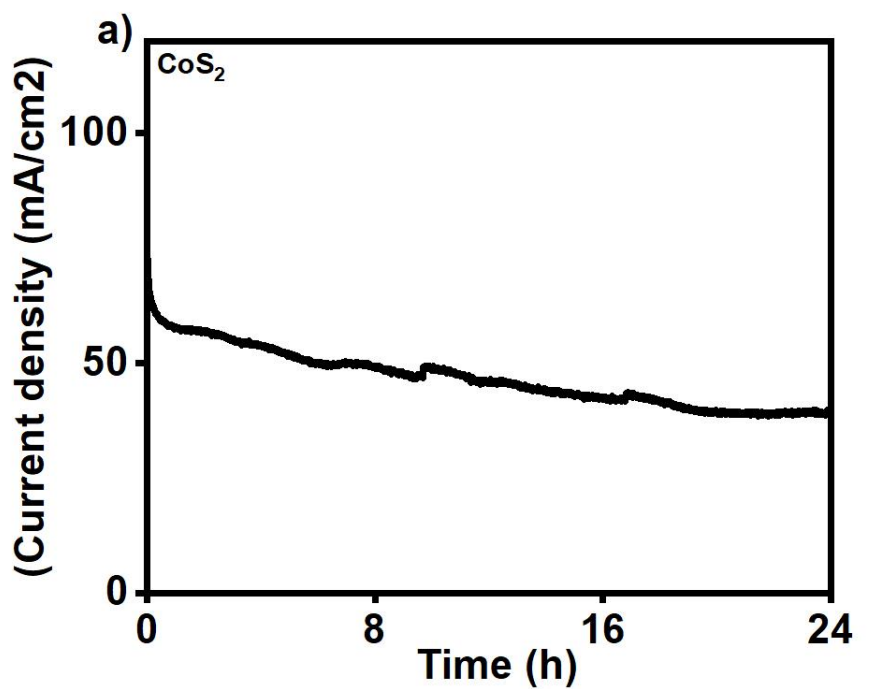
**Figure 18:** (a-c) Polarization curve stability over 10,000 cycles of all as-prepared samples.

The long-term electrochemical stability of $CoS_2$, $NiS_2$, and $FeS_2$ electrocatalysts toward the urea oxidation reaction was assessed through 24-hour chronoamperometry tests conducted in 1 M KOH containing urea. The current density versus time profiles, shown in **Figure 19 (a–c)**, reveal distinct differences in the durability of the materials under continuous electrochemical operation. Among the tested catalysts, $NiS_2$ **(Figure 19b)** exhibited the most stable current output, with an initial current density of 63 mA/cm² that declined only slightly to 50 mA/cm² after 24 hours. The minimal current loss and smooth decay indicate excellent electrochemical resilience, due to the chemical robustness of Ni-S bonds and their resistance to surface oxidation under alkaline oxidative conditions. $CoS_2$ **(Figure 19a)** also showed high initial current (58 mA/cm²), but a slightly more noticeable drop to 44 mA/cm² was observed, due to partial oxidation of cobalt species or slower surface stabilization during prolonged testing. Although $CoS_2$ maintained consistent performance, its larger fluctuation zones suggest a less uniform catalytic response compared to $NiS_2$. In contrast, $FeS_2$ **(Figure 19c)** displayed the lowest current retention. It started at 26 mA/cm² and decreased to 18 mA/cm² after 24 hours, indicating significant performance decay. This behavior may result from the susceptibility of iron sulfides to surface oxidation and leaching under high-potential alkaline conditions, which can compromise electrochemical conductivity and catalytic stability. Collectively, these results suggest that $NiS_2$ exhibits the highest stability toward UOR, followed by $CoS_2$ and $FeS_2$. The superior performance of $NiS_2$ in terms of current retention over extended operation demonstrates its potential as a durable and efficient anodic material for urea-assisted electrolysis systems.
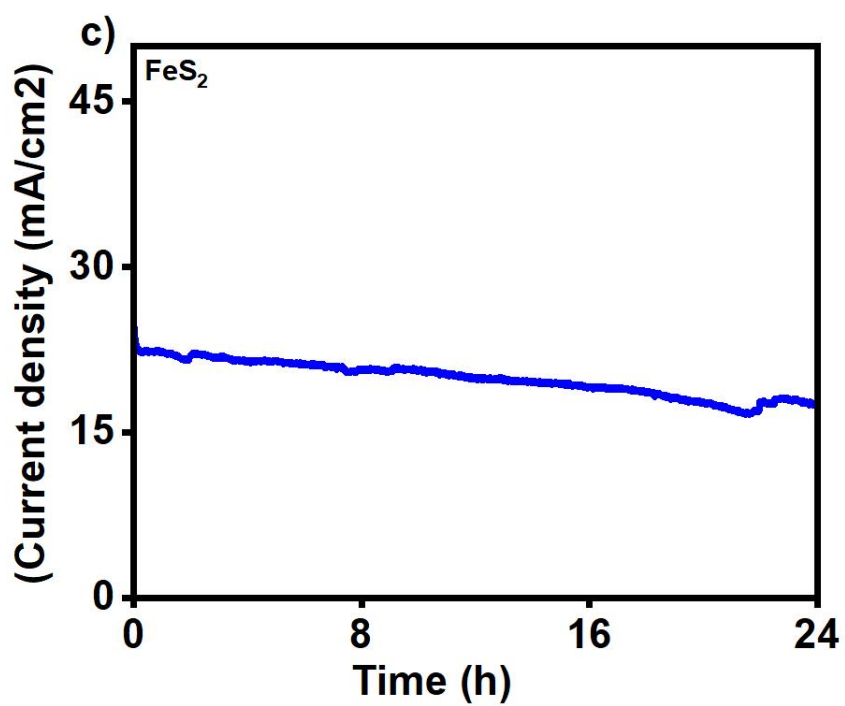
**Figure 19:** Chronoamperometry test for the water splitting process for 24h for the (a) $CoS_2$, (b) $NiS_2$ and (c) $FeS_2$, catalysts towards UOR.

**Table 3.** Electrocatalytic activity of metal (Fe/Co/Ni) based materials towards UOR.

| Material | Methods | Electrolyte | Onset potential | References |
|---|---|---|---|---|
| NiCoMo Sulfide Nanosheets | Microwave-assisted | 1 M KOH + 0.33 M Urea | 1.40 V | [114] |
| $CoS_2$ | Hydrothermal | 1 M KOH + 0.33 M Urea | 1.40 V | [115] |
| $NiS@Ni_3S_2/NiMoO_4$ | Hydrothermal | 1 M KOH + 0.33 M Urea | 1.30 V | [116] |
| $NiS/NiS_2$ | Hydrothermal | 1 M KOH + 0.33 M Urea | 1.36 V | [117] |
| $FeS_2$ | Microwave | 1 M KOH + 0.33 M Urea | 1.47 V | This work |
| $CoS_2$ | Microwave | 1 M KOH + 0.33 M Urea | 1.42 V | This work |
| $NiS_2$ | Microwave | 1 M KOH + 0.33 M Urea | 1.38 V | This work |

# CHAPTER IV

# CONCLUSION

In this work, nanostructured $CoS_2$, $NiS_2$, and $FeS_2$ electrocatalysts were successfully synthesized using a rapid microwave-assisted route followed by post-sulfurization at 450 °C under an inert atmosphere. X-ray diffraction confirmed the formation of highly crystalline cubic phases consistent with JCPDS #96-154-4895 ($CoS_2$), #96-901-2539 ($NiS_2$), and #96-901-5843 ($FeS_2$). Morphological analysis by SEM revealed that $CoS_2$ adopted micro spherical aggregates, $NiS_2$ formed uniform nanogranular clusters, and $FeS_2$ exhibited irregular flake-like structures. Elemental mapping via EDX confirmed homogeneous distributions of Co/S, Ni/S, and Fe/S in each material, validating successful sulfidation. Electrochemical investigations in 1 M KOH revealed that $NiS_2$ exhibited the highest activity toward the oxygen evolution reaction, requiring the lowest overpotential (260 mV at 10 mA/cm²) and displaying the smallest Tafel slope (42 mV/dec) and lowest charge transfer resistance (1.1 Ω). This performance is attributed to its rich $Ni^{2+}/Ni^{3+}$ redox transitions, high conductivity, and large electrochemical surface area . $CoS_2$ demonstrated moderate OER activity with an overpotential of 270 mV, a Tafel slope of 44 mV/dec, and a charge transfer resistance of 2.6 Ω. These values correlate with its micro spherical morphology and moderate surface roughness. In contrast, $FeS_2$ required the highest overpotential (300 mV), had the largest Tafel slope (45 mV/dec), and showed the highest

resistance (4.0 $\Omega$), consistent with its limited active site exposure and less favorable surface kinetics.

In the hydrogen evolution reaction, $CoS_2$ outperformed the other catalysts, exhibiting the lowest overpotential of 240 mV and the smallest Tafel slope of 179 mV/dec. Its metallic conductivity and near-optimal hydrogen binding energy contribute to efficient electron transfer and proton adsorption. $NiS_2$ followed with a slightly higher overpotential of 244 mV and a Tafel slope of 199 mV/dec but demonstrated the highest ECSA (1096 cm²) and roughness factor (2000), suggesting an abundance of accessible active sites. $FeS_2$ displayed the weakest HER activity with an overpotential of 275 mV and a Tafel slope of 236 mV/dec, owing to its semiconducting nature and sluggish charge transport.

Upon introducing 0.33 M urea into the electrolyte, a substantial enhancement in catalytic performance was observed for all samples during the urea oxidation reaction, due to the lower thermodynamic barrier of urea electrooxidation compared to OER. $NiS_2$ again emerged as the best-performing catalyst, delivering the lowest onset potential (1.38 V), the smallest Tafel slope (87.7 mV/dec), and the lowest interfacial resistance (1.1 $\Omega$) under UOR conditions. Its outstanding performance is attributed to the formation of electroactive NiOOH species, high conductivity, and interconnected nanostructure that promotes urea adsorption and dehydrogenation. $CoS_2$ showed competitive UOR activity with an onset potential of 1.42 V and a Tafel slope of 160 mV/dec, supported by its redox-active $Co^{2+}/Co^{3+}$ transitions and moderate charge transfer capability. $FeS_2$ showed the least favorable UOR performance with a high onset potential of 1.47 V, a Tafel slope of 143 mV/dec, and a high resistance of 4.0 $\Omega$, consistent with limited active site availability and poor conductivity. Electrochemical stability was evaluated through 1000-cycle LSV

tests and 24-hour chronoamperometry. All three materials demonstrated excellent durability across OER, HER, and UOR. $NiS_2$ showed the highest current retention during UOR (63-50 mA/cm²), followed by $CoS_2$ (58-44 mA/cm²), and $FeS_2$ (26-18 mA/cm²), supporting their structural integrity under extended operation.

In conclusion, $NiS_2$ is identified as the most efficient and bifunctional electrocatalyst, exhibiting excellent activity for both OER and UOR, along with robust performance in HER, due to its favorable redox behavior, high conductivity, and abundant active surface. $CoS_2$ stands out for HER performance and shows moderate activity in both OER and UOR, while $FeS_2$, although structurally stable, is limited by its electronic properties and intrinsic activity. This work demonstrates the potential of microwave-assisted synthesis for producing low-cost, scalable, and high-performance metal disulfide catalysts for integrated water and urea electrolysis systems aimed at sustainable hydrogen production and environmental remediation.

# REFERENCES

[1] D. Gielen, F. Boshell, D. Saygin, M. D. Bazilian, N. Wagner, and R. Gorini, "The role of renewable energy in the global energy transformation," *Energy Strategy Reviews*, vol. 24, pp. 38–50, Apr. 2019, doi: 10.1016/j.esr.2019.01.006.

[2] H. A. Bandal, A. R. Jadhav, A. H. Tamboli, and H. Kim, "Bimetallic iron cobalt oxide self-supported on Ni-Foam: An efficient bifunctional electrocatalyst for oxygen and hydrogen evolution reaction," *Electrochim Acta*, vol. 249, pp. 253–262, Sep. 2017, doi: 10.1016/j.electacta.2017.07.178.

[3] H. A. Bandal, A. R. Jadhav, A. H. Tamboli, and H. Kim, "Bimetallic iron cobalt oxide self-supported on Ni-Foam: An efficient bifunctional electrocatalyst for oxygen and hydrogen evolution reaction," *Electrochim Acta*, vol. 249, pp. 253–262, Sep. 2017, doi: 10.1016/j.electacta.2017.07.178.

[4] I. Dincer, "Green methods for hydrogen production," *Int J Hydrogen Energy*, vol. 37, no. 2, pp. 1954–1971, Jan. 2012, doi: 10.1016/j.ijhydene.2011.03.173.

[5] R. L. Reaño, "Assessment of environmental impact and energy performance of rice husk utilization in various biohydrogen production pathways," *Bioresour Technol*, vol. 299, p. 122590, Mar. 2020, doi: 10.1016/j.biortech.2019.122590.

[6] W. Yaseen *et al.*, "Ni-Fe-Co based mixed metal/metal-oxides nanoparticles encapsulated in ultrathin carbon nanosheets: A bifunctional electrocatalyst for overall water splitting," *Surfaces and Interfaces*, vol. 26, p. 101361, Oct. 2021, doi: 10.1016/j.surfin.2021.101361.

[7] S. Koohi-Fayegh and M. A. Rosen, "A review of energy storage types, applications and recent developments," *J Energy Storage*, vol. 27, p. 101047, Feb. 2020, doi: 10.1016/j.est.2019.101047.

[8] X. Luo, J. Wang, M. Dooner, and J. Clarke, "Overview of current development in electrical energy storage technologies and the application potential in power system operation," *Appl Energy*, vol. 137, pp. 511–536, Jan. 2015, doi: 10.1016/j.apenergy.2014.09.081.

[9] M. M. Rahman, A. O. Oni, E. Gemechu, and A. Kumar, "Assessment of energy storage technologies: A review," *Energy Convers Manag*, vol. 223, p. 113295, Nov. 2020, doi: 10.1016/j.enconman.2020.113295.

[10] W. Zhang, M. Liu, X. Gu, Y. Shi, Z. Deng, and N. Cai, "Water Electrolysis toward Elevated Temperature: Advances, Challenges and Frontiers," *Chem Rev*, vol. 123, no. 11, pp. 7119–7192, Jun. 2023, doi: 10.1021/acs.chemrev.2c00573.

[11]   B. Pivovar, "Catalysts for fuel cell transportation and hydrogen related uses," *Nat Catal*, vol. 2, no. 7, pp. 562–565, Jul. 2019, doi: 10.1038/s41929-019-0320-9.

[12]   C. Higman and S. Tam, "Advances in Coal Gasification, Hydrogenation, and Gas Treating for the Production of Chemicals and Fuels," *Chem Rev*, vol. 114, no. 3, pp. 1673–1708, Feb. 2014, doi: 10.1021/cr400202m.

[13]   P. Mondal, G. S. Dang, and M. O. Garg, "Syngas production through gasification and cleanup for downstream applications — Recent developments," *Fuel Processing Technology*, vol. 92, no. 8, pp. 1395–1410, Aug. 2011, doi: 10.1016/j.fuproc.2011.03.021.

[14]   A. Basile, S. Liguori, and A. Iulianelli, "Membrane reactors for methane steam reforming (MSR)," in *Membrane Reactors for Energy Applications and Basic Chemical Production*, Elsevier, 2015, pp. 31–59. doi: 10.1016/B978-1-78242-223-5.00002-9.

[15]   D. P. Harrison, "Sorption-Enhanced Hydrogen Production: A Review," *Ind Eng Chem Res*, vol. 47, no. 17, pp. 6486–6501, Sep. 2008, doi: 10.1021/ie800298z.

[16]   Z. Li, P. Wei, and G. Wang, "Recent Advances on Perovskite Electrocatalysts for Water Oxidation in Alkaline Medium," *Energy & Fuels*, vol. 36, no. 19, pp. 11724–11744, Oct. 2022, doi: 10.1021/acs.energyfuels.2c02236.

[17]   D. Yao, L. Gu, B. Zuo, S. Weng, S. Deng, and W. Hao, "A strategy for preparing high-efficiency and economical catalytic electrodes toward overall water splitting," *Nanoscale*, vol. 13, no. 24, pp. 10624–10648, 2021, doi: 10.1039/D1NR02307A.

[18]   C. Hu, L. Zhang, and J. Gong, "Recent progress made in the mechanism comprehension and design of electrocatalysts for alkaline water splitting," *Energy Environ Sci*, vol. 12, no. 9, pp. 2620–2645, 2019, doi: 10.1039/C9EE01202H.

[19]   S. Lokesh and R. Srivastava, "Advanced Two-Dimensional Materials for Green Hydrogen Generation: Strategies toward Corrosion Resistance Seawater Electrolysis─Review and Future Perspectives," *Energy & Fuels*, vol. 36, no. 22, pp. 13417–13450, Nov. 2022, doi: 10.1021/acs.energyfuels.2c02013.

[20]   C. Hu, L. Zhang, and J. Gong, "Recent progress made in the mechanism comprehension and design of electrocatalysts for alkaline water splitting," *Energy Environ Sci*, vol. 12, no. 9, pp. 2620–2645, 2019, doi: 10.1039/C9EE01202H.

[21]   S.-C. Ke, R. Chen, G.-H. Chen, and X.-L. Ma, "Mini Review on Electrocatalyst Design for Seawater Splitting: Recent Progress and Perspectives," *Energy & Fuels*,

vol. 35, no. 16, pp. 12948–12956, Aug. 2021, doi: 10.1021/acs.energyfuels.1c02056.

[22] Md. N. Uddin and W. M. A. W. Daud, "Technological Diversity and Economics: Coupling Effects on Hydrogen Production from Biomass," *Energy & Fuels*, vol. 28, no. 7, pp. 4300–4320, Jul. 2014, doi: 10.1021/ef5007808.

[23] M. Ganapathy, Y. Hsu, J. Thomas, L.-Y. Chen, C.-T. Chang, and V. Alagan, "Preparation of SrTiO$_3$/Bi$_2$S$_3$ Heterojunction for Efficient Photocatalytic Hydrogen Production," *Energy & Fuels*, vol. 35, no. 18, pp. 14995–15004, Sep. 2021, doi: 10.1021/acs.energyfuels.1c00979.

[24] A. Bolt, I. Dincer, and M. Agelin-Chaab, "A Review of Unique Aluminum–Water Based Hydrogen Production Options," *Energy & Fuels*, vol. 35, no. 2, pp. 1024–1040, Jan. 2021, doi: 10.1021/acs.energyfuels.0c03674.

[25] D. Ding, J. Huang, X. Deng, and K. Fu, "Recent Advances and Perspectives of Nanostructured Amorphous Alloys in Electrochemical Water Electrolysis," *Energy & Fuels*, vol. 35, no. 19, pp. 15472–15488, Oct. 2021, doi: 10.1021/acs.energyfuels.1c02706.

[26] F. Zhang and Q. Wang, "Redox-Mediated Water Splitting for Decoupled H$_2$ Production," *ACS Mater Lett*, vol. 3, no. 5, pp. 641–651, May 2021, doi: 10.1021/acsmaterialslett.1c00074.

[27] Y. Yan, B. Xia, Z. Xu, and X. Wang, "Recent Development of Molybdenum Sulfides as Advanced Electrocatalysts for Hydrogen Evolution Reaction," *ACS Catal*, vol. 4, no. 6, pp. 1693–1705, Jun. 2014, doi: 10.1021/cs500070x.

[28] Q. Zhu, Y. Qu, D. Liu, K. W. Ng, and H. Pan, "Two-Dimensional Layered Materials: High-Efficient Electrocatalysts for Hydrogen Evolution Reaction," *ACS Appl Nano Mater*, vol. 3, no. 7, pp. 6270–6296, Jul. 2020, doi: 10.1021/acsanm.0c01331.

[29] D.-H. Yang, Y. Tao, X. Ding, and B.-H. Han, "Porous organic polymers for electrocatalysis," *Chem Soc Rev*, vol. 51, no. 2, pp. 761–791, 2022, doi: 10.1039/D1CS00887K.

[30] S. Wang, A. Lu, and C.-J. Zhong, "Hydrogen production from water electrolysis: role of catalysts," *Nano Converg*, vol. 8, no. 1, p. 4, Dec. 2021, doi: 10.1186/s40580-021-00254-x.

[31] I. C. Man *et al.*, "Universality in Oxygen Evolution Electrocatalysis on Oxide Surfaces," *ChemCatChem*, vol. 3, no. 7, pp. 1159–1165, Jul. 2011, doi: 10.1002/cctc.201000397.

[32] T. R. Cook, D. K. Dogutan, S. Y. Reece, Y. Surendranath, T. S. Teets, and D. G. Nocera, "Solar Energy Supply and Storage for the Legacy and Nonlegacy Worlds," *Chem Rev*, vol. 110, no. 11, pp. 6474–6502, Nov. 2010, doi: 10.1021/cr100246c.

[33] D. Strmcnik *et al.*, "Improving the hydrogen oxidation reaction rate by promotion of hydroxyl adsorption," *Nat Chem*, vol. 5, no. 4, pp. 300–306, Apr. 2013, doi: 10.1038/nchem.1574.

[34] C. Feng, M. B. Faheem, J. Fu, Y. Xiao, C. Li, and Y. Li, "Fe-Based Electrocatalysts for Oxygen Evolution Reaction: Progress and Perspectives," *ACS Catal*, vol. 10, no. 7, pp. 4019–4047, Apr. 2020, doi: 10.1021/acscatal.9b05445.

[35] N.-T. Suen, S.-F. Hung, Q. Quan, N. Zhang, Y.-J. Xu, and H. M. Chen, "Electrocatalysis for the oxygen evolution reaction: recent development and future perspectives," *Chem Soc Rev*, vol. 46, no. 2, pp. 337–365, 2017, doi: 10.1039/C6CS00328A.

[36] J. K. Nørskov *et al.*, "Origin of the Overpotential for Oxygen Reduction at a Fuel-Cell Cathode," *J Phys Chem B*, vol. 108, no. 46, pp. 17886–17892, Nov. 2004, doi: 10.1021/jp047349j.

[37] I. C. Man *et al.*, "Universality in Oxygen Evolution Electrocatalysis on Oxide Surfaces," *ChemCatChem*, vol. 3, no. 7, pp. 1159–1165, Jul. 2011, doi: 10.1002/cctc.201000397.

[38] J. K. Nørskov, F. Abild-Pedersen, F. Studt, and T. Bligaard, "Density functional theory in surface chemistry and catalysis," *Proceedings of the National Academy of Sciences*, vol. 108, no. 3, pp. 937–943, Jan. 2011, doi: 10.1073/pnas.1006652108.

[39] W. Zhang, W. Lai, and R. Cao, "Energy-Related Small Molecule Activation Reactions: Oxygen Reduction and Hydrogen and Oxygen Evolution Reactions Catalyzed by Porphyrin- and Corrole-Based Systems," *Chem Rev*, vol. 117, no. 4, pp. 3717–3797, Feb. 2017, doi: 10.1021/acs.chemrev.6b00299.

[40] A. Sivanantham, P. Ganesan, A. Vinu, and S. Shanmugam, "Surface Activation and Reconstruction of Non-Oxide-Based Catalysts Through in Situ Electrochemical Tuning for Oxygen Evolution Reactions in Alkaline Media," *ACS Catal*, vol. 10, no. 1, pp. 463–493, Jan. 2020, doi: 10.1021/acscatal.9b04216.

[41] K. Zeng and D. Zhang, "Recent progress in alkaline water electrolysis for hydrogen production and applications," *Prog Energy Combust Sci*, vol. 36, no. 3, pp. 307–326, Jun. 2010, doi: 10.1016/j.pecs.2009.11.002.

[42] B. You, G. Han, and Y. Sun, "Electrocatalytic and photocatalytic hydrogen evolution integrated with organic oxidation," *Chemical Communications*, vol. 54, no. 47, pp. 5943–5955, 2018, doi: 10.1039/C8CC01830H.

[43] A. N. Rollinson, J. Jones, V. Dupont, and M. V. Twigg, "Urea as a hydrogen carrier: a perspective on its potential for safe, sustainable and long-term energy supply," *Energy Environ Sci*, vol. 4, no. 4, p. 1216, 2011, doi: 10.1039/c0ee00705f.

[44] T. Guo *et al.*, "Enabling the full exposure of Fe2P@NixP heterostructures in tree-branch-like nanoarrays for promoted urea electrolysis at high current densities," *Chemical Engineering Journal*, vol. 417, p. 128067, Aug. 2021, doi: 10.1016/j.cej.2020.128067.

[45] Y. Cheng, X. Xiao, X. Guo, H. Yao, and H. Pang, "Synthesis of 'Quasi-Ce-MOF' Electrocatalysts for Enhanced Urea Oxidation Reaction Performance," *ACS Sustain Chem Eng*, vol. 8, no. 23, pp. 8675–8680, Jun. 2020, doi: 10.1021/acssuschemeng.0c01800.

[46] X. Hu, J. Zhu, J. Li, and Q. Wu, "Urea Electrooxidation: Current Development and Understanding of Ni-Based Catalysts," *ChemElectroChem*, vol. 7, no. 15, pp. 3211–3228, Aug. 2020, doi: 10.1002/celc.202000404.

[47] S. Kanwal, N. Raheem, M. Q. Mehmood, M. Zubair, and L. K. Ang, "Characterization of field emission from random nano-structured surface in using fractional field emission models," *J Appl Phys*, vol. 136, no. 7, Aug. 2024, doi: 10.1063/5.0220388.

[48] A. M. Abuamr *et al.*, "Characterization of field emission from oxidized copper emitters," *Phys Scr*, vol. 99, no. 10, p. 105029, Oct. 2024, doi: 10.1088/1402-4896/ad7232.

[49] J. Epp, "X-ray diffraction (XRD) techniques for materials characterization," in *Materials Characterization Using Nondestructive Evaluation (NDE) Methods*, Elsevier, 2016, pp. 81–124. doi: 10.1016/B978-0-08-100040-3.00004-3.

[50] W.-W. Zhao *et al.*, "Improved Oxygen Reduction Reaction Activity of Nanostructured CoS $_2$ through Electrochemical Tuning," *ACS Appl Energy Mater*, vol. 2, no. 12, pp. 8605–8614, Dec. 2019, doi: 10.1021/acsaem.9b01527.

[51] Y. Bai, J. Yeom, M. Yang, S.-H. Cha, K. Sun, and N. A. Kotov, "Universal Synthesis of Single-Phase Pyrite FeS $_2$ Nanoparticles, Nanowires, and Nanosheets," *The Journal of Physical Chemistry C*, vol. 117, no. 6, pp. 2567–2573, Feb. 2013, doi: 10.1021/jp3111106.

[52] H. Pang *et al.*, "Microwave-assisted synthesis of NiS2 nanostructures for supercapacitors and cocatalytic enhancing photocatalytic H2 production," *Sci Rep*, vol. 4, no. 1, p. 3577, Jan. 2014, doi: 10.1038/srep03577.

[53] J. Zhang *et al.*, "Activating and Optimizing Activity of CoS $_2$ for Hydrogen Evolution Reaction through the Synergic Effect of N Dopants and S Vacancies," *ACS Energy Lett*, vol. 2, no. 5, pp. 1022–1028, May 2017, doi: 10.1021/acsenergylett.7b00270.

[54] C. Zhao, D. Li, and Y. Feng, "Size-controlled hydrothermal synthesis and high electrocatalytic performance of CoS2 nanocatalysts as non-precious metal cathode materials for fuel cells," *J Mater Chem A Mater*, vol. 1, no. 18, p. 5741, 2013, doi: 10.1039/c3ta10296c.

[55] W. Chen, T. Li, Q. Hu, C. Li, and H. Guo, "Hierarchical CoS2@C hollow microspheres constructed by nanosheets with superior lithium storage," *J Power Sources*, vol. 286, pp. 159–165, Jul. 2015, doi: 10.1016/j.jpowsour.2015.03.154.

[56] Y. Li *et al.*, "Construction of Heterostructured NiS/NiSe2 and their application in electrocatalytic water splitting," *Int J Hydrogen Energy*, vol. 66, pp. 286–293, May 2024, doi: 10.1016/j.ijhydene.2024.04.101.

[57] A. G. Oshchepkov, G. Braesch, A. Bonnefont, E. R. Savinova, and M. Chatenet, "Recent Advances in the Understanding of Nickel-Based Catalysts for the Oxidation of Hydrogen-Containing Fuels in Alkaline Media," *ACS Catal*, vol. 10, no. 13, pp. 7043–7068, Jul. 2020, doi: 10.1021/acscatal.0c00101.

[58] P. Liu, J. Li, Y. Lu, and B. Xiang, "Facile synthesis of NiS2 nanowires and its efficient electrocatalytic performance for hydrogen evolution reaction," *Int J Hydrogen Energy*, vol. 43, no. 1, pp. 72–77, Jan. 2018, doi: 10.1016/j.ijhydene.2017.11.096.

[59] S. A. Kadam *et al.*, "Ferromagnetic Hybrid 2D FeS/FeS $_2$ Nanostructures as Electrocatalysts for the Hydrogen Evolution Reaction," *ACS Appl Nano Mater*, vol. 7, no. 23, pp. 27566–27578, Dec. 2024, doi: 10.1021/acsanm.4c05598.

[60] D. Jasion, J. M. Barforoush, Q. Qiao, Y. Zhu, S. Ren, and K. C. Leonard, "Low-Dimensional Hyperthin FeS $_2$ Nanostructures for Efficient and Stable Hydrogen

Evolution Electrocatalysis," *ACS Catal*, vol. 5, no. 11, pp. 6653–6657, Nov. 2015, doi: 10.1021/acscatal.5b01637.

[61]    Mohd. Khalid, A. M. B. Honorato, H. Varela, and L. Dai, "Multifunctional electrocatalysts derived from conducting polymer and metal organic framework complexes," *Nano Energy*, vol. 45, pp. 127–135, Mar. 2018, doi: 10.1016/j.nanoen.2017.12.045.

[62]    P. Luo *et al.*, "Targeted Synthesis of Unique Nickel Sulfide (NiS, NiS$_2$) Microarchitectures and the Applications for the Enhanced Water Splitting System," *ACS Appl Mater Interfaces*, vol. 9, no. 3, pp. 2500–2508, Jan. 2017, doi: 10.1021/acsami.6b13984.

[63]    S. Anantharaj, S. R. Ede, K. Sakthikumar, K. Karthick, S. Mishra, and S. Kundu, "Recent Trends and Perspectives in Electrochemical Water Splitting with an Emphasis on Sulfide, Selenide, and Phosphide Catalysts of Fe, Co, and Ni: A Review," *ACS Catal*, vol. 6, no. 12, pp. 8069–8097, Dec. 2016, doi: 10.1021/acscatal.6b02479.

[64]    L.-L. Feng *et al.*, "High-Index Faceted Ni$_3$S$_2$ Nanosheet Arrays as Highly Active and Ultrastable Electrocatalysts for Water Splitting," *J Am Chem Soc*, vol. 137, no. 44, pp. 14023–14026, Nov. 2015, doi: 10.1021/jacs.5b08186.

[65]    Y. Kang *et al.*, "Identification of Interface Structure for a Topological CoS$_2$ Single Crystal in Oxygen Evolution Reaction with High Intrinsic Reactivity," *ACS Appl Mater Interfaces*, vol. 14, no. 17, pp. 19324–19331, May 2022, doi: 10.1021/acsami.1c24966.

[66]    S. A. Kadam *et al.*, "Ferromagnetic Hybrid 2D FeS/FeS$_2$ Nanostructures as Electrocatalysts for the Hydrogen Evolution Reaction," *ACS Appl Nano Mater*, vol. 7, no. 23, pp. 27566–27578, Dec. 2024, doi: 10.1021/acsanm.4c05598.

[67]    D. Jasion, J. M. Barforoush, Q. Qiao, Y. Zhu, S. Ren, and K. C. Leonard, "Low-Dimensional Hyperthin FeS$_2$ Nanostructures for Efficient and Stable Hydrogen Evolution Electrocatalysis," *ACS Catal*, vol. 5, no. 11, pp. 6653–6657, Nov. 2015, doi: 10.1021/acscatal.5b01637.

[68]    L. Xing *et al.*, "3D hierarchical local heterojunction of MoS2/FeS2 for enhanced microwave absorption," *Chemical Engineering Journal*, vol. 379, p. 122241, Jan. 2020, doi: 10.1016/j.cej.2019.122241.

[69]    Mohd. Khalid, A. M. B. Honorato, H. Varela, and L. Dai, "Multifunctional electrocatalysts derived from conducting polymer and metal organic framework

complexes," *Nano Energy*, vol. 45, pp. 127–135, Mar. 2018, doi: 10.1016/j.nanoen.2017.12.045.

[70]   Y. Ma *et al.*, "Cobalt Disulfide Nanoparticles Embedded in Porous Carbonaceous Micro-Polyhedrons Interlinked by Carbon Nanotubes for Superior Lithium and Sodium Storage," *ACS Nano*, vol. 12, no. 7, pp. 7220–7231, Jul. 2018, doi: 10.1021/acsnano.8b03188.

[71]   X. Huang and Z. Nan, "Porous 2D FeS2 nanosheets as a peroxidase mimic for rapid determination of H2O2," *Talanta*, vol. 216, p. 120995, Aug. 2020, doi: 10.1016/j.talanta.2020.120995.

[72]   M. Feng, J. Huang, Y. Peng, C. Huang, X. Yue, and S. Huang, "Tuning Electronic Structures of Transition Metal Carbides to Boost Oxygen Evolution Reactions in Acidic Medium," *ACS Nano*, vol. 16, no. 9, pp. 13834–13844, Sep. 2022, doi: 10.1021/acsnano.2c02099.

[73]   D. Jasion, J. M. Barforoush, Q. Qiao, Y. Zhu, S. Ren, and K. C. Leonard, "Low-Dimensional Hyperthin FeS $_2$ Nanostructures for Efficient and Stable Hydrogen Evolution Electrocatalysis," *ACS Catal*, vol. 5, no. 11, pp. 6653–6657, Nov. 2015, doi: 10.1021/acscatal.5b01637.

[74]   M. Wang, L. Zhang, Y. He, and H. Zhu, "Recent advances in transition-metal-sulfide-based bifunctional electrocatalysts for overall water splitting," *J Mater Chem A Mater*, vol. 9, no. 9, pp. 5320–5363, 2021, doi: 10.1039/D0TA12152E.

[75]   S. Anantharaj and S. Noda, "Appropriate Use of Electrochemical Impedance Spectroscopy in Water Splitting Electrocatalysis," *ChemElectroChem*, vol. 7, no. 10, pp. 2297–2308, May 2020, doi: 10.1002/celc.202000515.

[76]   N. Zhang *et al.*, "Surface Activation and Ni-S Stabilization in NiO/NiS $_2$ for Efficient Oxygen Evolution Reaction," *Angewandte Chemie International Edition*, vol. 61, no. 35, Aug. 2022, doi: 10.1002/anie.202207217.

[77]   D. Jasion, J. M. Barforoush, Q. Qiao, Y. Zhu, S. Ren, and K. C. Leonard, "Low-Dimensional Hyperthin FeS $_2$ Nanostructures for Efficient and Stable Hydrogen Evolution Electrocatalysis," *ACS Catal*, vol. 5, no. 11, pp. 6653–6657, Nov. 2015, doi: 10.1021/acscatal.5b01637.

[78]   S. Anantharaj, S. R. Ede, K. Sakthikumar, K. Karthick, S. Mishra, and S. Kundu, "Recent Trends and Perspectives in Electrochemical Water Splitting with an Emphasis on Sulfide, Selenide, and Phosphide Catalysts of Fe, Co, and Ni: A Review," *ACS Catal*, vol. 6, no. 12, pp. 8069–8097, Dec. 2016, doi: 10.1021/acscatal.6b02479.

[79]  Z. W. Seh, J. Kibsgaard, C. F. Dickens, I. Chorkendorff, J. K. Nørskov, and T. F. Jaramillo, "Combining theory and experiment in electrocatalysis: Insights into materials design," *Science (1979)*, vol. 355, no. 6321, Jan. 2017, doi: 10.1126/science.aad4998.

[80]  N. Zhang *et al.*, "Surface Activation and Ni-S Stabilization in NiO/NiS $_2$ for Efficient Oxygen Evolution Reaction," *Angewandte Chemie International Edition*, vol. 61, no. 35, Aug. 2022, doi: 10.1002/anie.202207217.

[81]  S. Trasatti, "Surface science and electrochemistry: concepts and problems," *Surf Sci*, vol. 335, pp. 1–9, Jul. 1995, doi: 10.1016/0039-6028(95)00446-7.

[82]  M. Li *et al.*, "Structural engineering of Fe-doped Ni2P nanosheets arrays for enhancing bifunctional electrocatalysis towards overall water splitting," *Appl Surf Sci*, vol. 536, p. 147909, Jan. 2021, doi: 10.1016/j.apsusc.2020.147909.

[83]  A. Toloei, V. Stoilov, and D. Northwood, "The Relationship Between Surface Roughness and Corrosion," in *Volume 2B: Advanced Manufacturing*, American Society of Mechanical Engineers, Nov. 2013. doi: 10.1115/IMECE2013-65498.

[84]  J. Lin *et al.*, "Defect-Rich Heterogeneous MoS $_2$ /NiS $_2$ Nanosheets Electrocatalysts for Efficient Overall Water Splitting," *Advanced Science*, vol. 6, no. 14, Jul. 2019, doi: 10.1002/advs.201900246.

[85]  D. Jasion, J. M. Barforoush, Q. Qiao, Y. Zhu, S. Ren, and K. C. Leonard, "Low-Dimensional Hyperthin FeS $_2$ Nanostructures for Efficient and Stable Hydrogen Evolution Electrocatalysis," *ACS Catal*, vol. 5, no. 11, pp. 6653–6657, Nov. 2015, doi: 10.1021/acscatal.5b01637.

[86]  Z. Zhang, C. Wu, L. Ji, and D. Zhou, "One-pot synthesis of pyrite type FeS 2 /C by microwave heating method and its electrochemical properties for oxygen evolution." [Online]. Available: https://ssrn.com/abstract=4105052

[87]  K. Pan, Y. Zhai, J. Zhang, and K. Yu, "FeS2/C Nanowires as an Effective Catalyst for Oxygen Evolution Reaction by Electrolytic Water Splitting," *Materials*, vol. 12, no. 20, p. 3364, Oct. 2019, doi: 10.3390/ma12203364.

[88]  B. Wang *et al.*, "A microwave-assisted bubble bursting strategy to grow Co8FeS8/CoS heterostructure on rearranged carbon nanotubes as efficient electrocatalyst for oxygen evolution reaction," *J Power Sources*, vol. 449, p. 227561, Feb. 2020, doi: 10.1016/j.jpowsour.2019.227561.

[89]   B. Yang, X. Ding, L. Feng, and M. Zhang, "NiS2/NiS/Mn2O3 Nanofibers with Enhanced Oxygen Evolution Reaction Activity," *Molecules*, vol. 29, no. 16, p. 3892, Aug. 2024, doi: 10.3390/molecules29163892.

[90]   Y. Tu *et al.*, "Synthesis and catalytic mechanism for NiS/NiS2/NC nanoparticles towards oxygen reduction reaction and oxygen evolution reaction," *Electrochim Acta*, vol. 470, p. 143346, Dec. 2023, doi: 10.1016/j.electacta.2023.143346.

[91]   S. Zhang *et al.*, "Microwave-assisted synthesis of amorphous NiS 2 catalysts with superior activity for the electro-oxidation of methanol." [Online]. Available: https://ssrn.com/abstract=4173292

[92]   N. Mushtaq *et al.*, "A facile and simple microwave-assisted synthesis method for mesoporous ultrathin iron sulfide nanosheets as an efficient bifunctional electrocatalyst for overall water splitting," *Dalton Transactions*, vol. 51, no. 16, pp. 6285–6292, 2022, doi: 10.1039/D2DT00019A.

[93]   X. Zhao *et al.*, "CoS2 hybridized Mo-doped VS4 core-shell three-dimensional nanoarrays for efficient hydrogen evolution reaction," *J Alloys Compd*, vol. 1020, p. 179346, Mar. 2025, doi: 10.1016/j.jallcom.2025.179346.

[94]   D. Strmcnik, P. P. Lopes, B. Genorio, V. R. Stamenkovic, and N. M. Markovic, "Design principles for hydrogen evolution reaction catalyst materials," *Nano Energy*, vol. 29, pp. 29–36, Nov. 2016, doi: 10.1016/j.nanoen.2016.04.017.

[95]   J. K. Nørskov *et al.*, "Trends in the Exchange Current for Hydrogen Evolution," *J Electrochem Soc*, vol. 152, no. 3, p. J23, 2005, doi: 10.1149/1.1856988.

[96]   A. Alshoaibi *et al.*, "NiS/NiS2-embedded sulfur-doped porous graphitic carbon nitride nanosheets as an efficient catalyst for 4-nitrophenol reduction," *Diam Relat Mater*, vol. 153, p. 112110, Mar. 2025, doi: 10.1016/j.diamond.2025.112110.

[97]   T. Wang *et al.*, "Electronic structure modulation of NiS 2 by transition metal doping for accelerating the hydrogen evolution reaction," *J Mater Chem A Mater*, vol. 7, no. 9, pp. 4971–4976, 2019, doi: 10.1039/C8TA11286J.

[98]   V. D. Nithya, "Recent advances in CoSe2 electrocatalysts for hydrogen evolution reaction," *Int J Hydrogen Energy*, vol. 46, no. 73, pp. 36080–36102, Oct. 2021, doi: 10.1016/j.ijhydene.2021.08.157.

[99]   T. Wang *et al.*, "Electronic structure modulation of NiS 2 by transition metal doping for accelerating the hydrogen evolution reaction," *J Mater Chem A Mater*, vol. 7, no. 9, pp. 4971–4976, 2019, doi: 10.1039/C8TA11286J.

[100] N. Zhang *et al.*, "Surface Activation and Ni-S Stabilization in NiO/NiS $_2$ for Efficient Oxygen Evolution Reaction," *Angewandte Chemie International Edition*, vol. 61, no. 35, Aug. 2022, doi: 10.1002/anie.202207217.

[101] H. Pang *et al.*, "Microwave-assisted synthesis of NiS2 nanostructures for supercapacitors and cocatalytic enhancing photocatalytic H2 production," *Sci Rep*, vol. 4, no. SREP03577, Jan. 2014, doi: 10.1038/srep03577.

[102] D. Xu *et al.*, "In Situ Formation of CoS2 Hollow Nanoboxes via Ion-Exchange for High-Performance Microwave Absorption," *Nanomaterials*, vol. 12, no. 16, p. 2876, Aug. 2022, doi: 10.3390/nano12162876.

[103] J. Wu, Y. Liang, P. Bai, S. Zheng, and L. Chen, "Microwave-assisted synthesis of pyrite FeS $_2$ microspheres with strong absorption performance," *RSC Adv*, vol. 5, no. 80, pp. 65575–65582, 2015, doi: 10.1039/C5RA14197D.

[104] W. Wang, W. Wang, Y. Xu, X. Ren, X. Liu, and Z. Li, "Synthesis of Ni3S4/NiS2/FeS2 nanoparticles for hydrogen and oxygen evolution reaction," *Appl Surf Sci*, vol. 560, p. 149985, Sep. 2021, doi: 10.1016/j.apsusc.2021.149985.

[105] M. Zhong, W. Li, C. Wang, and X. Lu, "Synthesis of hierarchical nickel sulfide nanotubes for highly efficient electrocatalytic urea oxidation," *Appl Surf Sci*, vol. 575, p. 151708, Feb. 2022, doi: 10.1016/j.apsusc.2021.151708.

[106] K. Ji *et al.*, "MoS2/CoS2 heterostructures embedded in N-doped carbon nanosheets towards enhanced hydrogen evolution reaction," *J Alloys Compd*, vol. 891, p. 161962, Jan. 2022, doi: 10.1016/j.jallcom.2021.161962.

[107] J. Yang *et al.*, "Metal-organic framework-derived FeS2/CoNiSe2 heterostructure nanosheets for highly-efficient oxygen evolution reaction," *Appl Surf Sci*, vol. 578, p. 152016, Mar. 2022, doi: 10.1016/j.apsusc.2021.152016.

[108] A. K. Satheesan *et al.*, "Current progress in layered double hydroxide-based electrocatalysts for urea oxidation: insights into strategies and mechanisms," *Chemical Communications*, vol. 61, no. 21, pp. 4092–4109, 2025, doi: 10.1039/D4CC05405A.

[109] K. Liu *et al.*, "Coupling interface constructions of flower-like structure MoSe2–NiWSe2 for efficient oxygen evolution reaction and urea oxidation reaction," *Mater Today Chem*, vol. 38, p. 102071, Jun. 2024, doi: 10.1016/j.mtchem.2024.102071.

[110] X. Zhang, S. Feizpoor, M. Humayun, and C. Wang, "Urea oxidation reaction electrocatalysts: Correlation of structure, activity, and selectivity," *Chem Catalysis*, vol. 4, no. 2, p. 100840, Feb. 2024, doi: 10.1016/j.checat.2023.100840.

[111]  Y. Zhang, H. Guo, M. Song, Z. Qiu, S. Wang, and L. Sun, "Hierarchical interfaces engineering-driven of the CoS2/MoS2/Ni3S2/NF electrode for high-efficient and stable oxygen evolution and urea oxidation reactions," *Appl Surf Sci*, vol. 617, p. 156621, Apr. 2023, doi: 10.1016/j.apsusc.2023.156621.

[112]  M. J. Wang *et al.*, "Fe $_3$ O $_4$ /FeS $_2$ heterostructures enable efficient oxygen evolution reaction," *J Mater Chem A Mater*, vol. 8, no. 28, pp. 14145–14151, 2020, doi: 10.1039/C9TA13775K.

[113]  F. Guo *et al.*, "Electrochemical impedance analysis of urea electro-oxidation mechanism on nickel catalyst in alkaline medium," *Electrochim Acta*, vol. 210, pp. 474–482, Aug. 2016, doi: 10.1016/j.electacta.2016.05.149.

[114]  B. Chen *et al.*, "Rapid Microwave Hydrothermal Synthesis of NiCoMo Sulfide Nanosheet Arrays for Hybrid Supercapacitors," *ACS Appl Nano Mater*, vol. 7, no. 8, pp. 9658–9667, Apr. 2024, doi: 10.1021/acsanm.4c01261.

[115]  S. Wei *et al.*, "CoS2 nanoneedle array on Ti mesh: A stable and efficient bifunctional electrocatalyst for urea-assisted electrolytic hydrogen production," *Electrochim Acta*, vol. 246, pp. 776–782, Aug. 2017, doi: 10.1016/j.electacta.2017.06.068.

[116]  L. Sha *et al.*, "A heterogeneous interface on NiS@Ni $_3$ S $_2$ /NiMoO $_4$ heterostructures for efficient urea electrolysis," *J Mater Chem A Mater*, vol. 8, no. 35, pp. 18055–18063, 2020, doi: 10.1039/D0TA04944A.

[117]  H. Liu, Z. Liu, F. Wang, and L. Feng, "Efficient catalysis of N doped NiS/NiS2 heterogeneous structure," *Chemical Engineering Journal*, vol. 397, p. 125507, Oct. 2020, doi: 10.1016/j.cej.2020.125507.